JOURNAL OF PETROLOGY

Journal of Petrology, 2017, Vol. 58, No. 5, 909–932
doi: 10.1093/petrology/egx040
Advance Access Publication Date: 17 August 2017
Original Article

OXFORD

The Thickness of the Mushy Layer on the Floor of the Skaergaard Magma Chamber at Apatite Saturation

Marian B. Holness[1]*, Christian Tegner[2], Troels F. D. Nielsen[3] and Bernard Charlier[4]

[1]Department of Earth Sciences, University of Cambridge, Downing Street, Cambridge CB2 3EQ, UK; [2]Centre of Earth System Petrology, Department of Geoscience, Aarhus University, Høegh-Guldbergs Gade 2, DK-8000 Aarhus C, Denmark; [3]Geological Survey of Denmark and Greenland, Øster Voldgade 10, DK-1350 Copenhagen K, Denmark; [4]Department of Geology, Université de Liège, B-4000 Sart Tilman, Belgium

*Corresponding author. E-mail: marian@esc.cam.ac.uk

Received October 29, 2015; Accepted June 28, 2017

ABSTRACT

We present a novel way of constraining the thickness of the crystal mush in fractionated layered intrusions using detailed microstructural analysis. The results are combined with geochemical data to create a snapshot of the crystal mush on the floor of the Skaergaard magma chamber in the period immediately before and after the saturation of the bulk liquid in apatite (the UZa–b boundary). The step-change in the fractional latent heat (that part of the total enthalpy budget associated with crystallization) accompanying the arrival of a new liquidus phase is recorded by a step-change in the median clinopyroxene–plagioclase–plagioclase dihedral angle, Θ_{cpp}, in fully solidified cumulates. Dihedral angles are formed during the last stages of solidification and hence the change of Θ_{cpp} associated with apatite-in marks a point close to the base of the mushy layer at the moment the bulk liquid became saturated in apatite, whereas the first appearance of abundant, homogeneously scattered, cumulus apatite crystals in the stratigraphy marks the top of the mushy layer at this moment. Comparison of the offset between these two markers in five widely spaced drill cores through the Skaergaard Layered Series suggests that the mushy layer was only a few metres thick at the UZa–b boundary in the centre and east of the floor, whereas it was ~100 m thick on the floor near the western margin. There is no correlation between the efficiency of liquid expulsion (as recorded by bulk-rock P_2O_5 concentrations and the stratigraphic distribution of reactive symplectites) and the recorded mush thickness at the moment of apatite saturation, suggesting that existing models of adcumulate formation that depend on mush thickness need to be reconsidered.

Key words: microstructure; cumulate; mush thickness; layered intrusion; dihedral angle

INTRODUCTION

When mafic magma stalls in a crustal magma chamber, cooling leads to crystallization and the formation of a mushy layer on the walls, roof and floor. Effective expulsion of evolved interstitial liquid from this mushy layer, particularly that forming on the chamber floor where the bulk of crystal accumulation occurs, creates adcumulates and drives fractionation of the remaining bulk magma (e.g. Nielsen *et al.*, 2015). Various processes have been suggested to account for the removal of evolved interstitial liquid, such as diffusion (Hess, 1960; Wager *et al.*, 1960), compositionally driven convection (Hess, 1972; Tait *et al.*, 1984; Tait & Jaupart, 1992) and compaction (Sparks *et al.*, 1985; Shirley, 1986; Tharp *et al.*, 1998; McKenzie, 2011). The effectiveness of these processes in driving fractionation is dependent on the physical properties (such as rheology and permeability) of the mushy layer and, in particular, on its thickness. The effectiveness of compositional convection (Tait & Jaupart, 1992) and compaction

(McKenzie, 2011) increases as the mushy layer becomes thicker. Conversely, the diffusive exchange of mass between the interstitial liquid and the overlying bulk liquid can play a significant role only in thin mushy layers (e.g. Wager *et al.*, 1960).

To date it has been difficult to constrain the thickness of the floor mushy layer from observations of fully solidified plutons, with estimates ranging from effectively zero (Morse, 1986) to hundreds of metres (e.g. Tait & Jaupart, 1992). In this contribution we argue that tight constraints can be placed on crystal mush thickness at localized stratigraphic horizons in layered intrusions, specifically those recording a change in the assemblage of liquidus minerals, using detailed microstructural analysis. The method links variations in the geometry of three-grain junctions (as quantified by the median clinopyroxene–plagioclase–plagioclase dihedral angle, Θ_{cpp}) associated with the arrival of new liquidus phases (see Holness *et al.*, 2007*a*, 2007*b*) with the spatial distribution of the new cumulus phase. We will argue that the thickness of the crystal mush on the floor of the Skaergaard magma chamber, at the point in its solidification history at which the bulk magma became saturated in apatite, varied between a few metres and ~100 m.

PREVIOUS ESTIMATES OF MUSHY LAYER THICKNESS

Model-based constraints on mush thickness include the work of Irvine (1980), who used the offset of compositional discontinuities by infiltration metasomatism across modal boundaries to estimate the thickness of the permeable (and compacting) mush zone in the Muskox intrusion to be of the order of several hundred metres. However, in a study of similar features in the Stillwater Intrusion, Boudreau & McCallum (1992) recognized that it is difficult to constrain the thickness of the compacting mush from such offsets. McKenzie (2011) constructed a simplified theoretical model of compaction, which, when applied to the observed stratigraphic variation of bulk-rock P_2O_5 concentration in the Skaergaard Layered Series, leads to a calculated mush thickness of 300 m. Metre-scale anti-correlations between rock density and the calculated fraction of trapped liquid in the Skaergaard Layered Series have been cited as evidence for a compacting mush of the order of tens of metres thick (Tegner *et al.*, 2009). Boudreau & Meurer (1999) suggested that the observed spatial distribution of platinum group elements (PGE) and Au in the mineralized horizons of the Skaergaard Triple Group is a consequence of the elements being concentrated by a chromatographic process involving upwards movement of volatile-rich fluids exsolved from crystallizing interstitial liquids in a compacting cumulate pile. Although their treatment is in terms of dimensionless distances, chromatographic behaviour would have had to operate through a mush of considerable (>60 m) thickness to account for the observed maximum offset of 60 m between the main Au and Pd horizons (Nielsen *et al.*, 2005). Model-based calculations of mush thickness such as these are dependent on assumptions about the physical properties of crystal mushy layers, such as their porosity, permeability and rheology. Little is known about these parameters or how they might vary with depth in the mush.

Field-based evidence for mush thickness includes disruption of layering owing to mechanical instability in the upper few metres of the Rum Eastern Layered Intrusion (Holness & Winpenny, 2009). Larger-scale slumping in the Lilloise intrusion led Chambers & Brown (1995) to suggest a mushy layer of >300 m on the chamber floor. Although there is potential to infer the rheological properties of a floor crystal mushy layer from its response to loading by blocks fallen from the roof, no published studies have yet used the range of observed behaviours to place firm constraints on mushy layer thickness: whereas Thompson & Patrick (1968) observed disruption and bending of layers 8 m below dense xenoliths in the Sarqata Qaqa intrusion of West Greenland, Irvine *et al.* (1998) found no unequivocal evidence for disruption of layering as a result of loading by xenoliths on the floor of the Skaergaard Intrusion. It has been suggested that field evidence for a thick mushy layer may be provided by discordant pipe-like structures, up to several hundred metres in height and containing late-stage minerals, in the Bushveld intrusion (Schiffries, 1982; Tait & Jaupart, 1992; Tegner *et al.*, 1994). If these are fossil channelways for interstitial liquids they suggest a mushy layer of considerable thickness (Tait & Jaupart, 1992), although their genesis is not yet understood.

Although much of the variation in published estimates of mush thickness is likely to be a consequence of the wide variety of size, morphology and cooling rate of the particular intrusion under consideration, some may be due to differences in the precise definition of the base of the mushy layer. Methods based on the permeability profile through the mush (such as those measuring or modelling transport distances of the interstitial liquid, e.g. Irvine, 1980; Boudreau & Meurer, 1999) will yield a different result from those based on observation of the depth to which the mushy layer responds to deformation or slumping (e.g. Brown *et al.*, 1987), as different physical properties are unlikely to vary with depth in the same way. Estimates of mush thickness based on the mobility of interstitial liquid may also be affected by the possibility that such liquid may be reactive and create its own flow pathways (e.g. Butcher *et al.*, 1985; Leuthold *et al.*, 2014). In this contribution we define the base of the mush to be that horizon at which all possible three-grain junctions between two grains of plagioclase and one of clinopyroxene have been created.

In texturally equilibrated liquid-bearing systems with low liquid–solid–solid dihedral angles and isotropic interfacial energies, the liquid remains interconnected down to vanishingly low porosities (Smith, 1964), and hence to the end-point of solidification. However, because the melt topology in solidifying gabbros is

unlikely to be in textural equilibrium (Holness *et al.*, 2012*a*) there is a finite porosity (the percolation threshold) below which the remaining melt no longer forms an interconnected network: at this point the remaining liquid is thus immobilized and trapped. Cheadle *et al.* (2004) showed that the percolation threshold occurs at 8–11 vol. % for non-texturally equilibrated systems. Examination of the progressive solidification of the crust of the Kilauea Iki lava lake (Holness *et al.*, 2012*a*) suggests that the clinopyroxene–plagioclase–plagioclase dihedral angle population in gabbros is completely formed when the rock is >90 vol. % solidified, suggesting that by this point in the solidification history (at least in gabbros that are not undergoing deformation) any remaining liquid is essentially immobile. The point at which all dihedral angles are formed can therefore act as a marker for the base of the mush.

MICROSTRUCTURAL INDICATORS OF SOLIDIFICATION TIMESCALES

Plagioclase grain shape

During interface-controlled growth, plagioclase grows as tabular grains (rather than dendrites or spherulites), with a shape controlled by the cooling rate via the differing response of the growth faces to changes in temperature (Holness, 2014, 2015). Rapid cooling results in most growth occurring on faces other than (010) [probably predominantly (100) and (001), e.g. Duchêne *et al.*, 2008], to form platy grains, whereas at slower cooling rates significant growth occurs on the (010) faces to form blocky grains. For rocks in which plagioclase is randomly oriented, this variation in shape can be quantified with no need for any underlying assumptions either about the 3D grain shape (see Higgins, 1994), or about relationships between shape and grain size, by using the average apparent aspect ratio, AR, of plagioclase as viewed in thin section (e.g. Meurer & Boudreau, 1998; Boorman *et al.*, 2004; Holness, 2014). Rocks containing generally equant plagioclase will have a low AR, whereas rocks containing generally more platy plagioclase will have a high AR. Values of AR in in the central parts of dolerite sills closely correlate with model crystallization time (Holness, 2014).

Dihedral angles

The geometry of clinopyroxene–plagioclase–plagioclase three-grain junctions in most gabbros and dolerites records processes active during solidification. Sub-solidus modification of the primary geometry created during the solidification of basaltic magma in the mid- to shallow crust is significant only in very fine-grained rocks that remained hot for a considerable time (e.g. the chill zones of large intrusions) (Holness *et al.*, 2012*a*).

The geometry of clinopyroxene–plagioclase–plagioclase three-grain junctions varies spatially within mafic intrusions. In essentially unfractionated bodies, such as sills, the median dihedral angle, Θ_{cpp}, varies smoothly and symmetrically, with higher values in the centre of the sill compared with the edges, correlating with the crystallization timescale (Holness *et al.*, 2012*b*). In fractionated bodies such as layered intrusions, Θ_{cpp} is constant over large stretches of stratigraphy, with stepwise changes associated with changes in the number of phases on the liquidus. An increase in the number of phases results in a stepwise increase in Θ_{cpp}, whereas Θ_{cpp} decreases when the number of liquidus phases decreases (Holness *et al.*, 2013).

The dihedral angle at any clinopyroxene–plagioclase–plagioclase junction is strongly affected by the extent to which the plagioclase (010) faces bounding the melt-filled pore grow during the last stages of solidification. Because proportionately more plagioclase growth occurs on (010) faces during slow cooling, populations of dihedral angles formed under these conditions have high median values (Holness, 2015). The stepwise changes of Θ_{cpp} observed in layered intrusions can thus be linked to changes in the absolute, local, cooling rate resulting from changes in the contribution of latent heat to the enthalpy budget (the fractional latent heat) that are associated with the addition or subtraction of phases from the liquidus assemblage (Wyllie, 1963; Morse, 2011; Holness *et al.*, 2013).

MICROSTRUCTURAL CONSTRAINTS ON MUSH THICKNESS

Mush thickness from consideration of primocryst abundance and grain size

For a well-mixed chamber such as Skaergaard, in which minerals of the same composition are crystallizing simultaneously on the walls, roof and floor (e.g. Salmonsen & Tegner, 2013), it is a reasonable assumption that the magma–mush interface is isothermal. For such a case, an indication of the mush structure may be obtained from a consideration of the stratigraphic variation in mode, morphology, and spatial distribution of a new liquidus phase immediately before and after it appears as a primocryst mineral. Porosity is likely to be high in the upper parts of the mush (50–60%: Wright *et al.*, 1968; Irvine, 1980; Shirley, 1986; Turbeville, 1993; Tegner *et al.*, 2009) and the composition of the interstitial liquid is close to that of the overlying bulk magma. For some time preceding the saturation of the bulk magma in the new liquidus phase, it is therefore likely that crystals of this new phase will nucleate and grow in the abundant pore space in the upper part of the mush (Hunter, 1996; Fig. 1a), closely spatially associated with late-stage interstitial phases. In the absence of compaction, the mode of the new liquidus phase (and the concentration of any compositional tracers such as P_2O_5 for cumulus apatite) would therefore increase over a greater stratigraphic distance in cumulates formed from a thick mushy layer compared with those that formed from a thin mushy layer. The morphology of the grains nucleating and growing in the upper parts of the mush is likely to be different from that of primocrysts of the

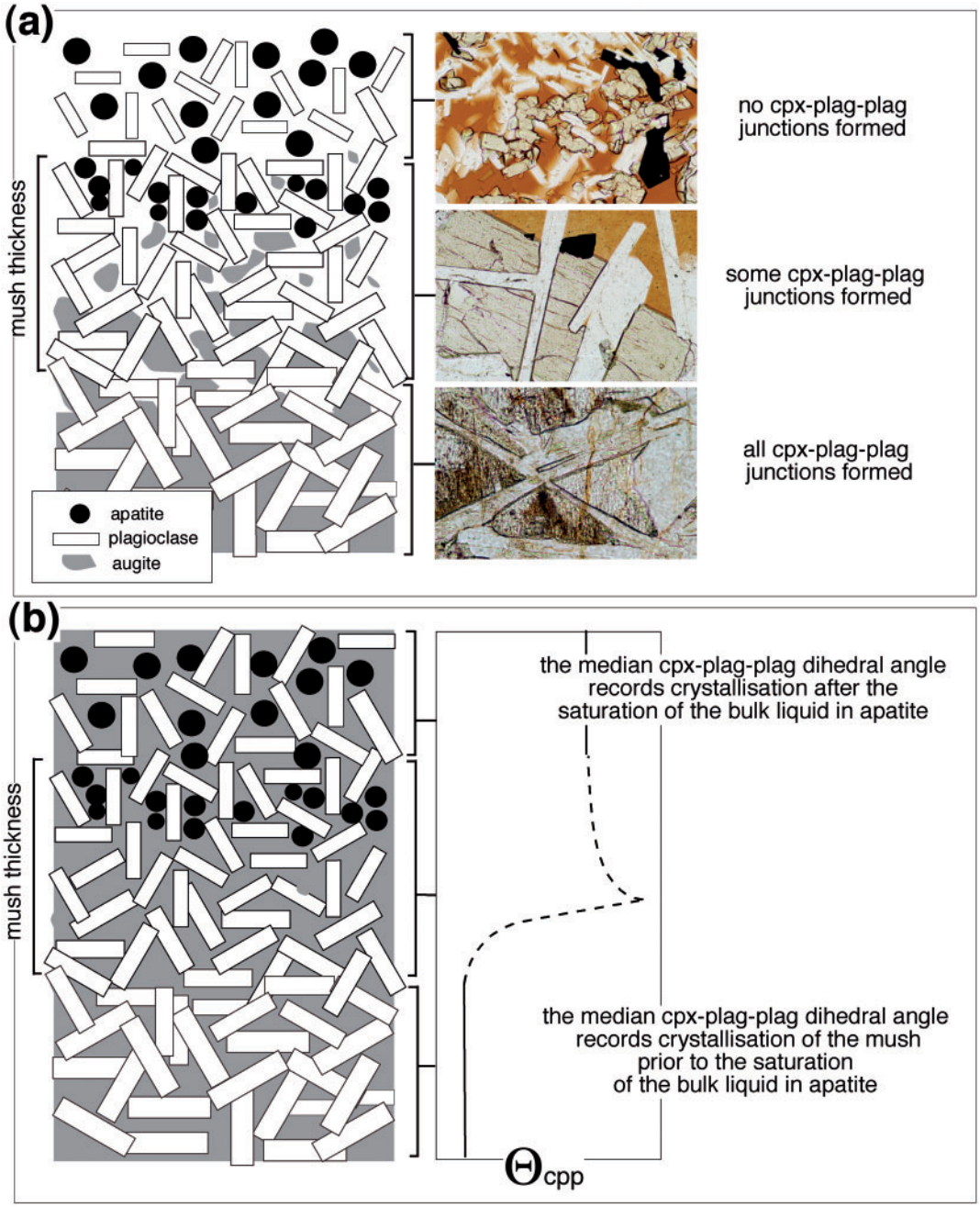

Fig. 1. Schematic illustrations of microstructural variation through a progressively solidifying mush, with photomicrographs illustrating what progressive solidification looks like in natural samples of the crust of the Kilauea Iki lava lake, with complete solidification illustrated by an image of the Portal Peak Sill (Antarctica). (a) A snapshot of the mush shortly after the saturation of the bulk magma in a new phase (depicted here as apatite). Immediately before the bulk liquid becomes saturated in apatite, apatite nucleates and grows in the highly porous upper layers of the mush. The number of clinopyroxene (augite)–plagioclase–plagioclase junctions increases with depth in the mush, until all possible junctions have been formed (which occurs when the mush is almost completely solid). The thickness of the mushy layer is given by the distance between the horizon at which mush is almost completely solid and the horizon where the first homogeneously distributed primocrysts of apatite are found. (b) Schematic illustration of the fully solidified cumulate pile. The horizon at which all possible clinopyroxene–plagioclase–plagioclase junctions were already formed at the moment the bulk liquid became saturated in apatite marks the stratigraphically highest point at which the value of Θ_{cpp} records the thermal conditions corresponding to a bulk liquidus assemblage without primocryst apatite. The highly schematic step-change (dashed part of the line) occurs in that part of the stratigraphy that comprised the mushy layer at the moment the bulk liquid became saturated in apatite. The mush thickness at this moment is recorded in the fully solidified cumulates as the stratigraphic separation between the base of the Θ_{cpp} step and the first appearance of homogeneously distributed and abundant apatite primocrysts.

same phase that grow directly from the bulk magma. Some minerals form large oikocrysts before their appearance as cumulus grains (e.g. Hunter, 1996), although other minerals, such as apatite, rarely form anhedral grains. Instead, they may grow as euhedral grains clustered in melt pockets bounded by primocryst grains of the earlier liquidus assemblage and associated with late-stage phases that crystallized from evolved liquid: in such a case the top of the mush is marked by the appearance of abundant and homogeneously distributed crystals of the new primocryst phase, which have no particular spatial association with late-stage phases.

If the arrival of the new phase is marked by an overabundance of nucleation (e.g. Morse, 1979, 2011), its first appearance as cumulus grains in the stratigraphy will be characterized by highly abundant small grains. An observed difference across the intrusion floor in the stratigraphic distance over which the nucleation density decreases, and the average grain size of the new phase increases, will thus point to spatial differences in crystal accumulation rate. In a well-mixed chamber, this change will occur over a greater stratigraphic distance in those parts of the floor in which the mush was rapidly accumulating (and hence thicker) compared with those parts of the floor where the mush was accumulating more slowly.

Mush thickness from plagioclase grain shape and dihedral angles

We can use the relationships between AR, dihedral angle and crystallization time of Holness *et al.* (2012*b*) and Holness (2014) to estimate mush thickness in solidifying intrusions. If it is assumed that crystal nucleation and growth occurs entirely *in situ*, plagioclase shape and dihedral angle are dependent on the time taken for the upwards-migrating solidification front at the base of the mush to move a distance equal to the thickness of the mush. Provided we can estimate the rate at which the solidification front moves, we can then use the observed plagioclase grain shape and dihedral angle to estimate mush thickness by relating the values of these parameters to the time taken to crystallize.

Mush thickness constrained using stepwise changes in Θ_{cpp}

More accurate measurements of mush thickness can be made at specific stratigraphic horizons using the stepwise increase in Θ_{cpp} caused by the increase in fractional latent heat (Holness *et al.*, 2007*a*, 2007*b*, 2009; Morse, 2011). The first appearance of the new primocrysts in the cumulate stratigraphy marks the top boundary of the mush at the instant the bulk magma becomes saturated with the new phase (Fig. 1a). The base of the Θ_{cpp} step marks the point at which the dihedral angle changes from the value associated with the old liquidus assemblage to that associated with the new liquidus assemblage (Fig. 1b), triggered by a change in the growth behaviour of interstitial plagioclase in response to a change in the local latent heat contribution to the enthalpy budget.

Because three-grain junction geometry is formed during solidification, the base of the step in Θ_{cpp} marks the point at which all possible clinopyroxene–plagioclase–plagioclase three-grain junctions were already formed at the moment the bulk liquid above the mushy layer became saturated in the new liquidus phase (Fig. 1). All possible clinopyroxene–plagioclase–plagioclase dihedral angles will be formed in solidifying orthocumulates (i.e. those cumulates containing abundant interstitial liquid, similar to the basalts of the Kilauea Iki crust) when ~10 vol. % liquid remains (Holness *et al.*, 2012*a*), although in rocks with a more adcumulate character dihedral angle formation will be complete only when the rock is closer to complete solidification. The base of the step therefore corresponds to the horizon at which the volume of remaining liquid had dropped below the permeability threshold (see Cheadle *et al.*, 2004), with much or all of the remaining liquid below this horizon likely to have been retained. The more adcumulate the rock, the more closely the stratigraphic position of the dihedral angle step corresponds to the horizon at which the mushy layer is fully solidified. The base of the step therefore provides a marker for the base of the crystal mush, and the mush thickness is recorded by the distance from the base of the step to the first appearance of the new liquidus phase in the cumulates (Fig. 1).

The effect of compaction

Although the relative positions of the various textural and compositional markers cannot be changed in the stratigraphy of the final, fully solidified cumulate, the absolute positions of the markers can be altered by melt expulsion (and volume decrease) owing to gravitationally driven compaction. Given that the primary porosity of an accumulating mushy layer is likely to be <60 vol. % and the minimum final porosity ~5 vol. % (Tegner *et al.*, 2009), the maximum possible effect of compaction is to reduce the apparent mush thickness recorded by microstructures in fully solidified cumulates by a factor of ~0·55.

GEOLOGICAL SETTING

The Skaergaard Intrusion (Fig. 2) formed from the injection of a large (8 km × 11 km × 4 km, Nielsen, 2004) body of relatively evolved tholeiitic basalt into a fault-bounded (Irvine *et al.*, 1998) space forming on the extending margin of East Greenland during the opening of the North Atlantic. The intrusion lies at the unconformity between Precambrian gneisses and an overlying sequence of Eocene plateau lavas (Wager & Deer, 1939) to which the Skaergaard magma is closely related (Nielsen, 2004; Jakobsen *et al.*, 2010). Once the chamber inflated to its final size (Holness *et al.*, 2007*a*, 2015)

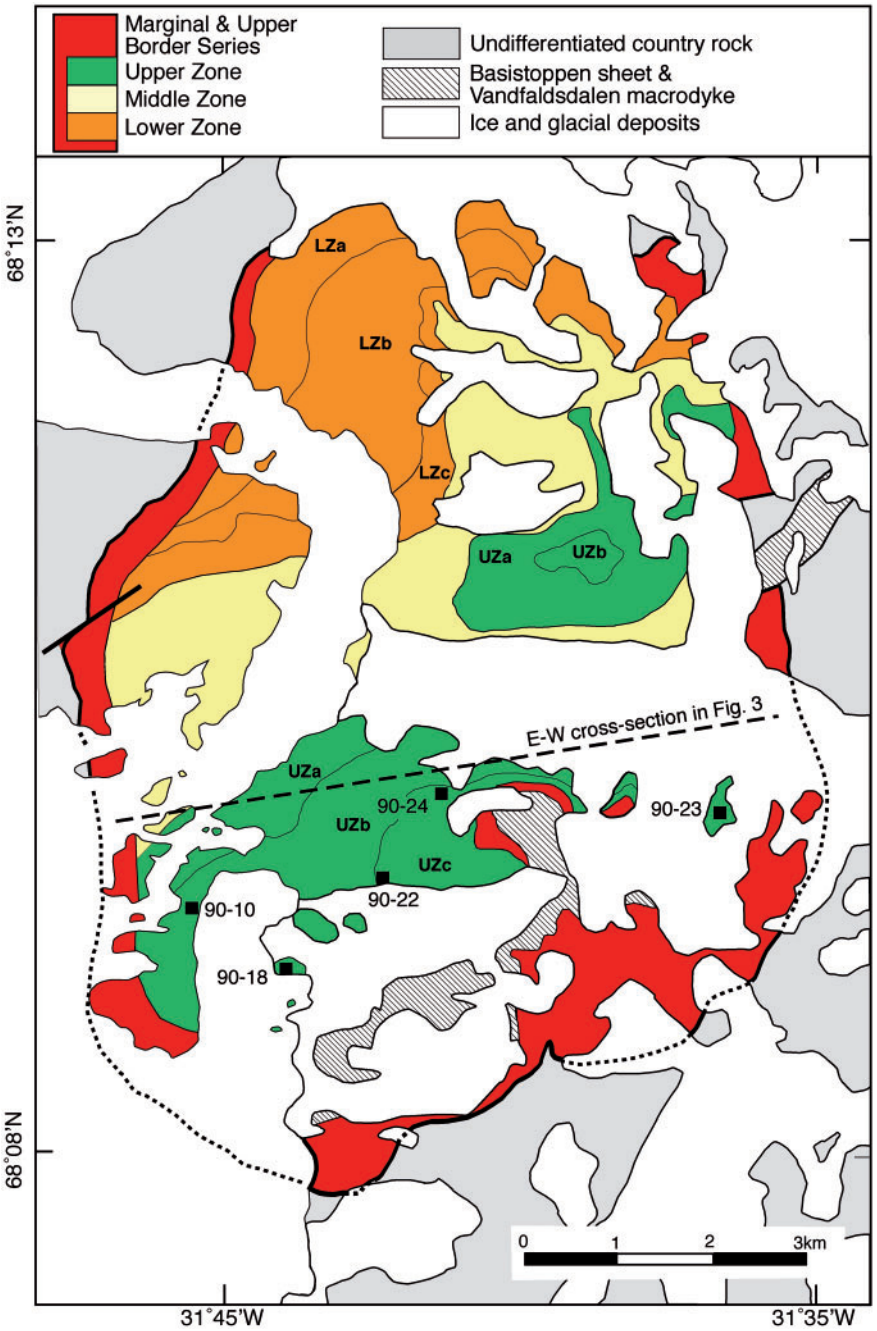

Fig. 2. Simplified geological map of the Skaergaard Intrusion, after McBirney (1989), showing the position of the five drill cores used in the present study. The line of cross-section shown in Fig. 3 is also shown.

it remained closed both to further magma replenishment and to eruption, crystallizing to form one of the world's best examples of extreme fractionation of a basaltic magma.

Solidification resulted in the formation of three series, first defined by Wager & Deer (1939): the (volumetrically dominant) Layered Series crystallized upwards from the floor; the Marginal Border Series (MBS) crystallized inwards from the (vertical) walls; the Upper Border Series (UBS) crystallized downwards from the roof. The Layered Series and Upper Border Series meet at the Sandwich Horizon. Progressive fractionation within the chamber resulted in these three series displaying a correlated series of changes in liquidus assemblage that permit the subdivision of each. The Layered Series is divided into Lower, Middle and Upper Zones based on the absence of cumulus olivine in the Middle Zone. The Lower Zone is subdivided into LZa (containing cumulus olivine and plagioclase), LZb (with cumulus augite) and LZc (with cumulus Fe–Ti oxides). The Upper Zone is also subdivided: the base of UZb defines the arrival of cumulus apatite, whereas the base of UZc marks the first appearance of the mosaic form of ferro-hedenbergite inverted from β-ferrobustamite.

The UBS (Salmonsen & Tegner, 2013; although see Naslund, 1984) and MBS (Hoover, 1989) can be similarly subdivided.

The upper part of the MZ is marked by a set of three macro-layers known as the Triple Group. These layers contain notable PGE and Au mineralization (Bird *et al.*, 1991; Andersen *et al.*, 1998; Holwell & Keays, 2014; Nielsen *et al.*, 2015). The thickness of the bowl-shaped Triple Group (Nielsen, 2004; Nielsen *et al.*, 2009; Svennevig & Guarnieri, 2012) and the spacing of the host rock layers are near constant across much of the floor [Appendices 1, 2, 3 and 5 of Nielsen *et al.* (2015)].

The thickness of UZa is shown in Fig. 3, determined from drill core. The data constraining the base of UZa (from Nielsen *et al.*, 2015) are relatively abundant, reflecting the greater outcrop area of UZa compared with UZb; the top of UZa is defined from only six cores. The distance of each drill core from the western contact was calculated using the great-circle distance between the two points assuming a spherical Earth and the profile constructed by projecting these distances onto a single east–west profile (shown in Fig. 2). The data are shown in Fig. 3 as absolute height relative to a horizon 400 m below present-day sea level. We show the total length of core between these two markers in each of the six cores, together with the length of gabbro in each core (i.e. subtracting from the first total the length taken up by later dolerite dykes). The large discrepancy between these two values for core 90-20 is caused by it intersecting a mafic dyke along a 110 m length of the hole. Although such a long section of dyke may have been created by the fortuitous intersection of the drill hole with an essentially parallel dyke, it may equally have been a consequence of the difficulty of getting the drill bit out of the dyke and back into the gabbro. We therefore suggest that the true thickness of UZa in the locality of core 90-20 is close to the total length, although the thickness of gabbro that was bypassed by the dyke is unknown.

The top of UZa is shown as a dashed line in Fig. 3, placed between the points showing the overall thickness and the thickness of gabbro. Regardless of whether we use the upper or lower measure of the UZa thickness, it varies from west to east, with the lowest values (~250 m) in the west, a maximum (~350 m) in, or near, the centre of the intrusion floor and a general reduction in thickness towards the eastern margin.

During the last stages of solidification, an extensive hydrothermal circulation system began to operate, particularly in the highly fractured plateau lavas that form the roof of the intrusion and the upper part of the eastern wall, leading to significant resetting of oxygen and hydrogen isotope ratios in the uppermost parts of the intrusion in the SE (Taylor & Forester, 1979). Most of the western wall of the intrusion is formed of relatively impermeable Precambrian gneiss, where significant meteoric water circulation was confined to major fracture zones (Taylor & Forester, 1979; Bird *et al.*, 1986; Bufe *et al.*, 2014).

Microstructures in the Skaergaard Layered Series

Holness (2015) reported a systematic variation of average apparent aspect ratio of plagioclase, AR, with stratigraphic height through the Layered Series (Fig. 4a). The lowest values of AR, and hence the most equant grains (as observed in thin section), are found at a stratigraphic height of ~2230 m [corresponding to UZa, using the stratigraphic correlations of Holness *et al.* (2007*b*)] in drill core 90-22 from the centre of the intrusion. This is consistent with thermal models of the intrusion (Norton & Taylor, 1979) and its contact aureole (Manning *et al.*, 1993; Bufe *et al.*, 2014), which suggest that this part of the stratigraphy experienced the slowest rate of cooling.

The sequential arrivals on the liquidus of the cumulus phases augite, Fe–Ti oxides and apatite are recorded by step-changes in Θ_{cpp} (Holness *et al.*, 2007*a*, 2007*b*,

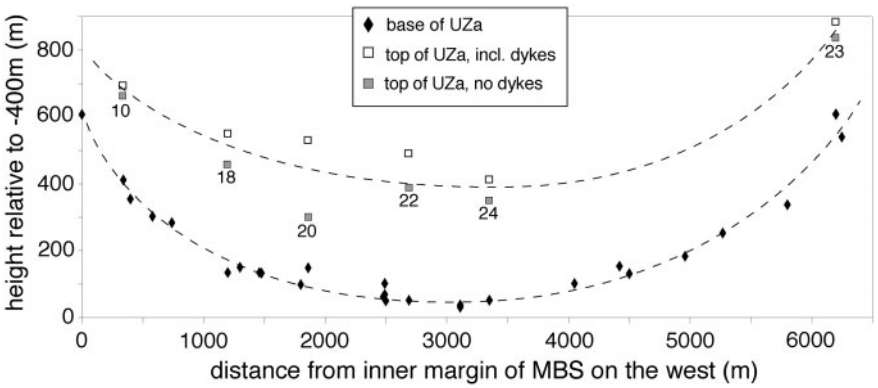

Fig. 3. The thickness of UZa across an east–west traverse (shown in Fig. 2), plotted as absolute height relative to a datum level 400 m below current sea-level. The base of UZa is taken as the upper contact of L3 (the topmost leucolayer of the Triple Group) and the top is marked by the arrival of cumulus apatite. All data from drill cores drilled in 1990, with the number of the drill core given (e.g. 18 denotes core 90-18). The data for the base of UZa are from Nielsen *et al.* (2015). Two points are plotted for the top of UZa in each of the cores containing this boundary: the upper point shows the entire thickness of UZa whereas the lower point shows the thickness of gabbro, omitting later dykes. The overall bowl shape of the layering and the greater thickness of UZa in the centre of the floor should be noted.

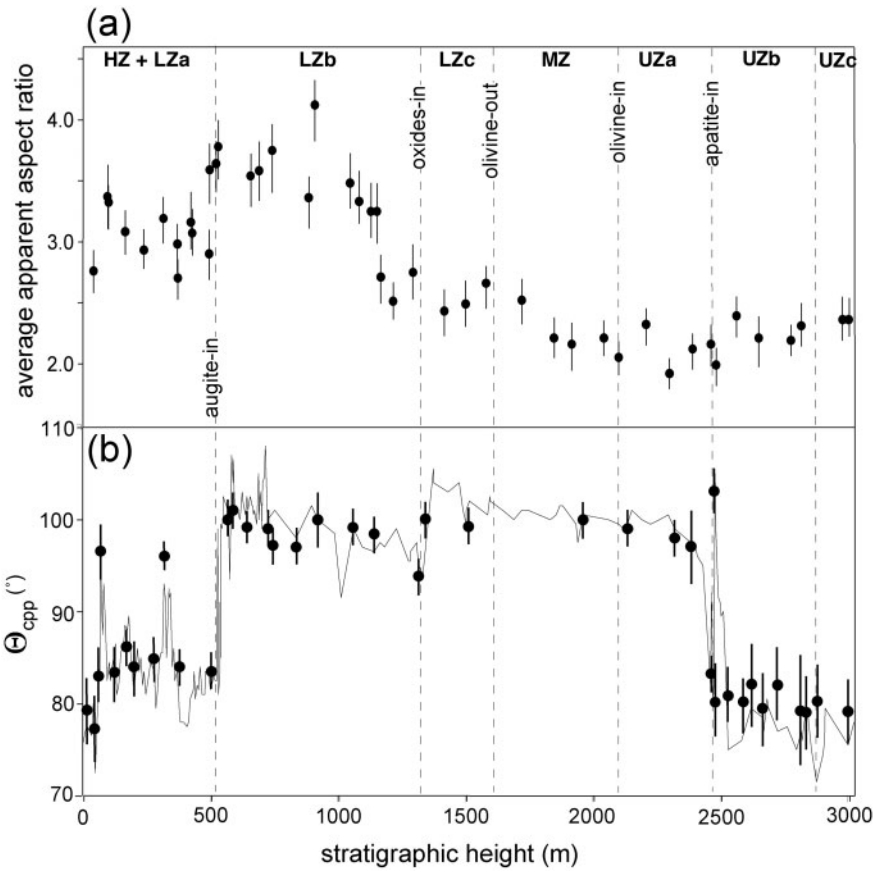

Fig. 4. Microstructural variation in the Skaergaard Layered Series. (a) Average apparent aspect ratio, AR, of plagioclase as a function of stratigraphic height, from Holness (2015). The stratigraphic correlation between samples is that of Holness *et al.* (2007*b*). (b) Stratigraphic variation of Θ_{cpp}, from Holness *et al.* (2013). The continuous line shows the data of Holness *et al.* (2007*b*), whereas the dots are those from Holness *et al.* (2013) based on larger measurement populations. The error bars show the 95% confidence intervals.

2013; Fig. 4b). For this study we concentrate on the step-change associated with apatite saturation. In drill core 90-22 Θ_{cpp} gradually reduces to 80° in the upper part of UZa, followed by an abrupt jump to $103 \pm 2{\cdot}5°$ marking the base of UZb (Holness *et al.*, 2007*b*, 2013, Figs 4b and 5a). These high values are not maintained and Θ_{cpp} decreases to ~90° over a few metres of stratigraphy. Holness *et al.* (2007*b*) interpreted this spike as indicative of a burst of crystallization related to temporary apatite over-saturation of the bulk magma, but it may be a result of the spike-like (i.e. transient) nature of the change in fractional latent heat (Holness *et al.*, 2009). Some 50 m above the Θ_{cpp} spike, Θ_{cpp} is in the range 75–80° until the Sandwich Horizon (Holness *et al.*, 2007*b*, 2013).

Values of 75–80° for Θ_{cpp} in much of UZb and in UZc are a consequence of three-grain junctions being formed by the meeting of planar augite–plagioclase grain boundaries that are commonly parallel to plagioclase growth faces (Fig. 6). This very distinctive microstructure is otherwise seen only in dolerite that solidified on time-scales of <10 years, in which the growth rate of the plagioclase (010) faces was so low that melt-filled pores in the plagioclase framework were filled entirely by augite, instead of a combination of augite and plagioclase (Holness, 2015). The gabbros of the Skaergaard UZ are coarse-grained and have low AR: they could not have solidified as quickly as dolerites. Instead, the cessation of growth on plagioclase (010) faces must have been because plagioclase simply did not grow in volumetrically significant amounts from the highly evolved liquids in the crystal mush during dihedral angle formation in this part of the stratigraphy (Holness, 2015). The distinctiveness of this newly described microstructure merits the coining of a new term to describe it. The similarity of the three-grain junction geometry to those observed in (relatively rapidly crystallized) dolerites, together with their coarse grain size, led Holness (2015) to suggest the name 'macro-dolerite' for these low-Θ_{cpp} gabbros.

The composition of late-stage liquids in the Skaergaard crystal mush

As pointed out in the previous section, because dihedral angles form during the last stages of solidification the composition of the late-stage interstitial liquid plays a significant role in their formation. Constraining this composition requires us to know not only the liquid line of descent of the bulk magma (which will control the

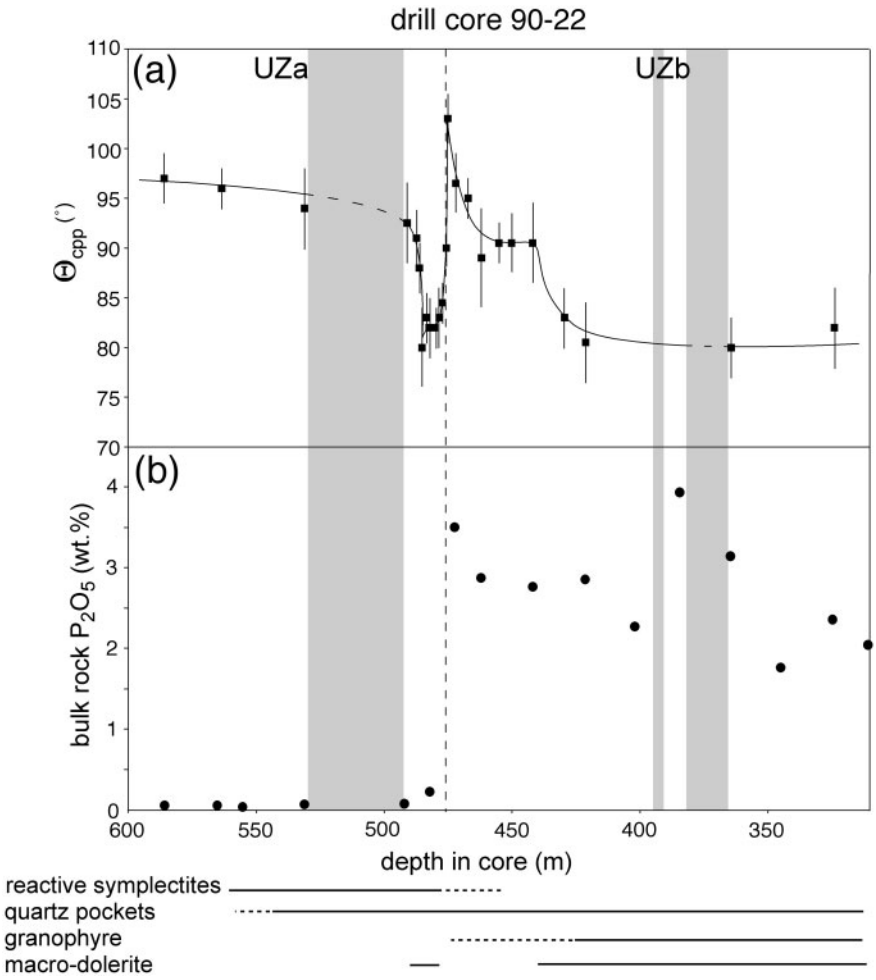

Fig. 5. (a) Variation of Θ_{cpp} in drill core 90-22, from Holness (2015). (b) The bulk-rock P_2O_5 concentration [data from Tegner *et al.* (2009)]. The arrival of cumulus apatite is shown as the dotted line at 475 m depth in core. The vertical grey bands show the stratigraphic position and extent of late-stage dykes [no distinction is made between mafic and (the rarer and thinner) granophyric dykes]. The continuous lines beneath the graph denote regions of the stratigraphy characterized by different late-stage microstructural features (shown in Fig. 7); the dotted ends to these lines denote stratigraphic regions where each late-stage feature is present but rare.

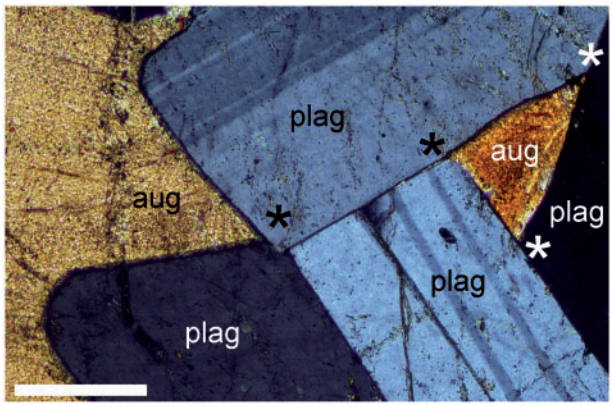

Fig. 6. Three-grain junctions in a sample from UZb (sample 98608 from the Harker Collection, University of Cambridge). All four clinopyroxene–plagioclase–plagioclase junctions shown (each with an asterisk adjacent) are formed by the meeting of planar clinopyroxene–plagioclase grain boundaries. aug, augite; plag, plagioclase. Crossed polars. Scale bar represents 200 μm.

initial composition of the interstitial liquid) but also the liquid line of descent within the mush, which may not be the same as that of the bulk. In particular, we need to know if the interstitial liquid encountered the two-liquid solvus and the consequences of such an encounter. The requisite information is preserved in the interstitial mineral assemblage and microstructures in the UZ cumulates, in the Sandwich Horizon and in the lowermost rocks of the UBS [into which late-stage liquids formed in the underlying Sandwich Horizon may have migrated (McBirney, 2002)].

There is considerable disagreement about the Skaergaard liquid line of descent, with support for Fe-enrichment in the last liquids (Wager, 1960; Brooks & Nielsen, 1978; McBirney & Naslund, 1990; Tegner, 1997; Jang *et al.*, 2001; Tegner & Cawthorn, 2010) contrasting with studies advocating progressive Si-enrichment (Hunter & Sparks, 1987, 1990; Toplis & Carroll, 1995, 1996; Irvine *et al.*, 1998). Based on mass balance of the intrusion (Nielsen, 2004) and average compositions,

Nielsen *et al.* (2009) suggested a liquid line of descent intermediate between the end-member Fenner (Fe-enrichment) and Bowen (Si-enrichment) trends, which results in a residual granophyric melt.

The picture is obscured by work supporting the preferential loss of an immiscible Si-rich conjugate from the interstitial liquid in the floor cumulates through much of the stratigraphy between LZc and UZa (Holness *et al.*, 2011). Such preferential loss of liquid from the floor mush has the potential not only to drive the liquid line of descent of the bulk magma towards Si-enrichment but also to leave an unrepresentatively Fe-rich bulk composition in the fully solidified floor sequence (Nielsen *et al.*, 2015).

Evidence for the preferential loss of a Si-rich conjugate and the destabilization of the remaining Fe-rich conjugate is provided by reactive symplectites of anorthitic plagioclase and olivine and/or clinopyroxene that replace primocrysts of plagioclase and, to a lesser extent, augite (Fig. 7a and b). These features are common from LZc to MZ, but gradually disappear over an ~200 m transition zone. In this zone, reactive symplectites are first joined by pockets of interstitial quartz, bounded by irregular plagioclase margins (Fig. 7c), and then disappear, to be replaced by coexisting pockets of granophyre (Fig. 7d) and patches of ilmenite intergrown with a variety of different minerals (Fig. 7e and f). This transition occurs within MZ near the margins of the intrusion, but in UZb at the centre of the floor [it is shown in fig. 5 of McBirney (1996) as the horizon at which granophyre becomes volumetrically significant]. The transition has been interpreted as marking the point above which silica-rich conjugate liquid (now solidified to granophyre) was no longer lost to the overlying bulk magma but was retained in the mush (Holness *et al.*, 2011).

Granophyre is always volumetrically more abundant than the coexisting ilmenite-rich intergrowths, which decrease in importance upwards through the stratigraphy, disappearing entirely above UZb. Ilmenite-rich intergrowths are absent in the Sandwich Horizon. This suggests that the bulk composition of the interstitial liquid moved towards the Si-rich side of the two-liquid field with progressive evolution, with the Fe-rich conjugate being totally consumed by crystallization leaving a single, Si-rich liquid to crystallize alone during the last stages of solidification, similar to the evolution inferred for the Sept Iles intrusion (Charlier *et al.*, 2011).

Despite the abundant plagioclase primocrysts in the Sandwich Horizon demonstrating that plagioclase was an important part of the assemblage crystallizing from the last remaining bulk magma, it has previously been argued that the macro-dolerite microstructure is a consequence of plagioclase not growing in volumetrically significant quantities from the late-stage interstitial liquid in UZ. That this is the case is supported by grain morphology: whereas olivine, ferro-augite and (inverted) β-ferrobustamite (Fig. 8a–d) all have irregular grain shapes indicating significant overgrowth from the interstitial liquid, the plagioclase grains in UZb and UZc are generally euhedral with little sign of overgrowth (Figs 7d and 8a, b; Namur *et al.*, 2014). Instead, plagioclase rhombs [sometimes with thin albitic rims pointing to limited overgrowth of the primocryst cores (Larsen & Tegner, 2006)] are surrounded by abundant granophyre. Plagioclase therefore cannot have crystallized in volumetrically important quantities from the late-stage granophyric liquid present in the upper parts of UZ and in the Sandwich Horizon.

It is possible that plagioclase crystallization was suppressed by the high H_2O contents of the late-stage liquid (e.g. Botcharnikov *et al.*, 2008). Sonnenthal (1992) presented evidence for the presence of an abundant, high-temperature, aqueous volatile phase in UZa. Gabbroic pegmatites, present throughout the Layered Series and the MBS and thought to have crystallized from pockets of residual liquid, contain primary magmatic amphibole (Larsen *et al.*, 1992; Larsen & Brooks, 1994). Larsen *et al.* (1992) described primary inclusions of saline aqueous fluid in interstitial phases such as quartz and apatite in the upper third of MZ, in UZ and in the Sandwich Horizon, as well as in gabbroic pegmatites. Larsen & Tegner (2006) showed that granophyric pockets throughout the Layered Series contain primary aqueous fluid inclusions.

CHOICE OF SAMPLES

Mineral exploration of the Triple Group has resulted in numerous drill cores being sunk through the upper part of the Layered Series, and many of these cores transect the UZa–b boundary. Five representative cores are housed in the Geological Museum in Copenhagen (Nielsen *et al.*, 2000). These include 90-22, 90-24 and 90-18 from the intrusion centre, with cores 90-10 and 90-23 from the west and east margins, respectively, of the chamber floor (Fig. 2). The petrology and geochemistry of core 90-22 have been described by Tegner (1997) and Tegner *et al.* (2009), and core 90-10 was described by Madsen (2005). All cores were drilled perpendicular to the layering in the intrusion (thus providing true measures of layer thickness), and generally contain later dykes of basalt or granophyre: logs of each core, showing the position of samples for which we report values of Θ_{cpp}, are shown in Fig. 9.

Sets of samples from these five drill cores, covering the UZa–b boundary, were examined for this study. Whereas 90-23 was sampled only on an exploratory basis, with sample spacings of 10–20 m, the other four were sampled with 0·5 m spacings within critical regions of interest.

Data are reported in Supplementary Data, Appendices 1 and 2 (supplementary data are available for downloading at http://www.petrology.oxfordjournals.org).

ANALYSIS METHODS

Dihedral angles

True dihedral angles were measured using a four-axis Leitz universal stage mounted on a James Swift

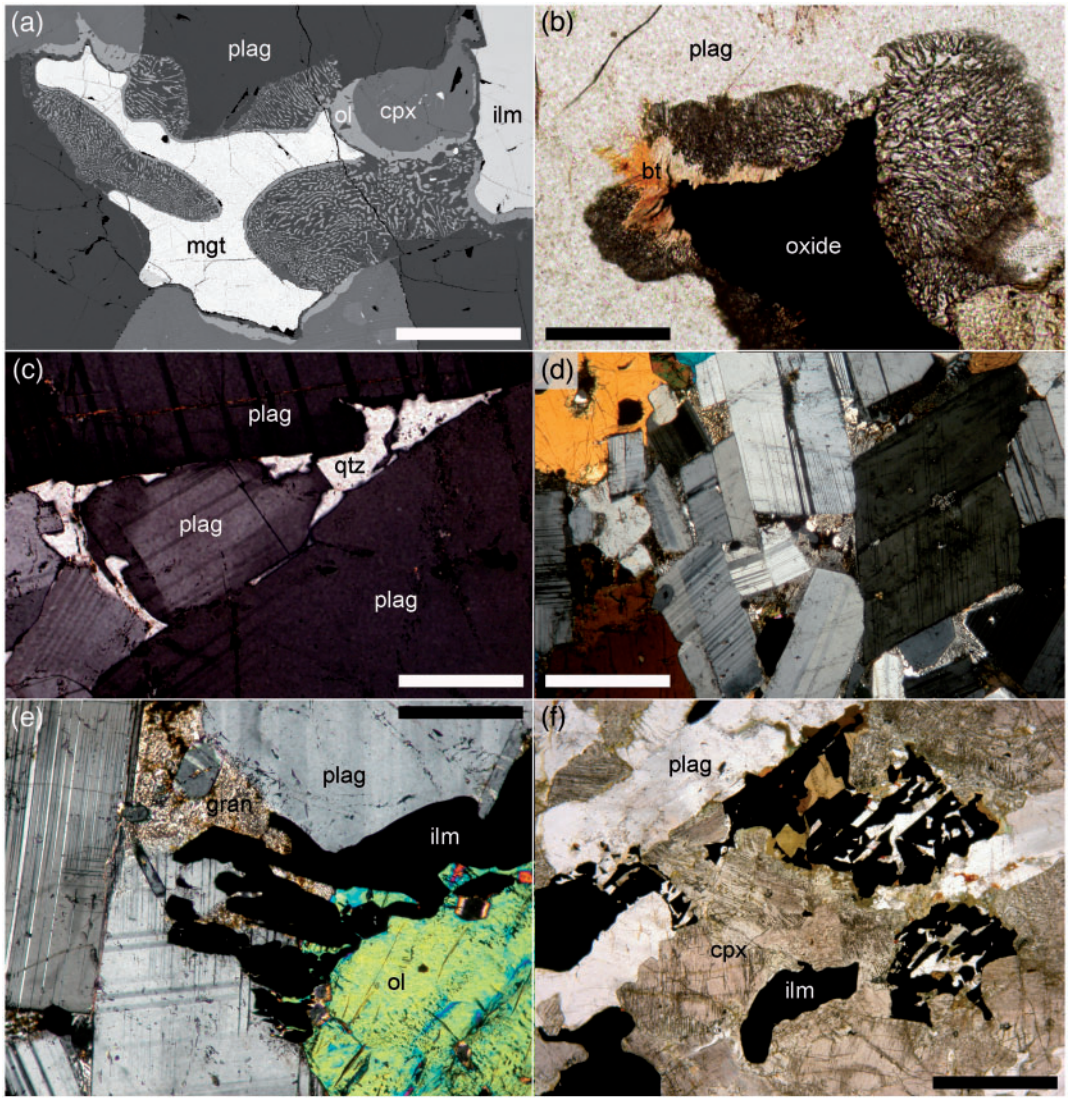

Fig. 7. Microstructures formed from the crystallization of late-stage liquids. (a) Back-scattered electron image of a reactive symplectite of anorthitic plagioclase and olivine (ol) replacing primocrysts of plagioclase and pyroxene. Sample 90-22 906.16. cpx, clinopyroxene; mgt, magnetite; ilm, ilmenite. Scale bar represents 500 μm. (b) A reactive symplectite of anorthitic plagioclase and clinopyroxene growing from an Fe–Ti oxide substrate, and replacing plagioclase primocrysts. The thin discontinuous rim of biotite (bt) separating the symplectite from the oxide substrate should be noted. Sample 90-22 893.6. Plane-polarized light. Scale bar represents 200 μm. (c) Interstitial grain of quartz (qtz) between plagioclase primocrysts. The highly irregular boundaries of the plagioclase grains and their albitic rims, denoting simultaneous growth of plagioclase and quartz from the interstitial liquid, should be noted. Sample 90-22 482.2. Crossed polars. Scale bar represents 200 μm. (d) Equant plagioclase with generally faceted margins indicative of little overgrowth from the interstitial liquid, much of which has crystallized as granophyre. Sample 90-22 87.7. Crossed polars. Scale bar represents 1 mm. (e) Interstitial pocket filled at the plagioclase-bounded end by granophyre and at the olivine-bounded end by an ilmenite-rich intergrowth. Sample 90-22 87.7. Crossed polars. Scale bar represents 500 μm. (f) Ilmenite intergrown with plagioclase and (brown) amphibole. Sample 90-22 993.28. Plane-polarized light. Scale bar represents 1 mm.

monocular optical microscope, with a UM32 Leitz objective and a × 10 eyepiece. The median value of a population of angles can be determined satisfactorily with only 25 measurements (Riegger & Van Vlack, 1960), although reduction of the uncertainty on the median to $<\pm$2–4° generally requires more than 50 measurements for those samples with a wide range of true angles (Holness, 2010). Tight constraints can be placed on the standard deviation of dihedral angle only as the population approaches 100 (Holness, 2010). For each sample, up to 100 individual measurements were made, although for a few their coarse grain size prevented measurement of more than 30 angles in a single thin section (no duplicates were made). Quoted uncertainties are the 2σ confidence intervals about the median calculated according to the method of Stickels & Hücke (1964).

Bulk-rock compositions

Bulk-rock compositions were determined at the University of Liège (samples from drill core 90-24) and at the University of Aarhus (all other drill core samples). Fused glasses for bulk-rock analysis were prepared by

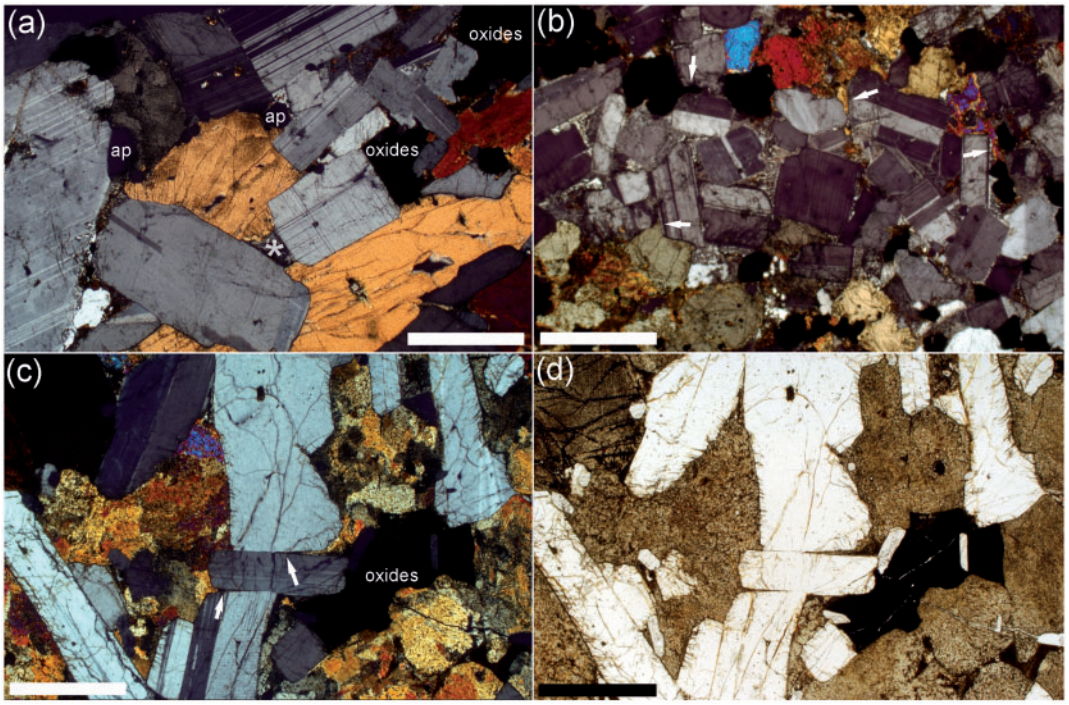

Fig. 8. Photomicrographs under crossed polars of microstructures typical of UZa and UZb. (a) Sample 98608 from UZb (Harker Collection, University of Cambridge), showing the euhedral, low aspect ratio plagioclase typical of this part of the intrusion. In the centre of the image, two grains of ferro-augite have distinct overgrowths that partially fill a previously melt-filled space between two euhedral plagioclase primocrysts, neither of which have shapes or compositional rims suggestive of significant interstitial overgrowth. The remaining space (marked with an asterisk) is filled with granophyre. Euhedral apatite primocrysts are denoted 'ap'. (b) Sample 98639 from UBS on Nunatak 1 (Harker Collection, University of Cambridge). The low aspect ratio and euhedral morphology (denoting no overgrowth from the interstitial liquid) of the plagioclase should be noted. Rims formed during growth from the interstitial liquid are thin and scarce. Plagioclase primocrysts are surrounded by abundant granophyre, with overgrowth of primocrysts of oxide (arrowed at top left), and ferro-augite (examples are marked by arrows at top right, bottom left and centre right) partially infilling the melt-filled spaces surrounding the plagioclase. (c) Sample 48723 from the Sandwich Horizon; this is a sample of the Purple Band of Wager & Deer (1939). Under crossed polars the polycrystalline nature of the inverted β-ferrobustamite is clearly visible. At the centre of the image is a euhedral plagioclase primocryst that was surrounded on two sides by thin melt-filled films. These films are entirely (arrow to the right) or partially (arrow to the left) filled by interstitial overgrowth of the β-ferrobustamite. The remaining space is filled by granophyre. (d) Same field of view as (c) but with plane-polarized light. All scale bars represent 1 mm.

mixing 0·75 g ignited sample with 3·75 g of Fluore-X65 HP (a commercial flux from Socachim Fine Chemicals consisting of 66 wt % $Li_2B_4O_7$ and 34 wt % $LiBO_2$) in a 95Pt–5Au crucible. After fusion, the melt was poured into a red-hot, 32 mm 95Pt–5Au mould and quenched in air to a flat glass disc. The mass lost on ignition was determined by heating the powder in air in a muffle furnace at 950°C (University of Aarhus) or 1000°C (University of Liège) for 3 h.

At the University of Aarhus, major and trace element compositions were analysed on a PANalytical PW2400 X-ray spectrometer using SuperQ software. For the major elements we used a 3 kW Rh tube, operating at 50 kV and 55 mA using a Ge crystal for P. The detector was a gas flow proportional counter using P10 (10% methane in Ar) gas. At the University of Liège, major element compositions were determined using the ARL PERFORM-X 4200, with matrix corrections following the Lachance–Traill algorithm. Accuracy and reproducibility were evaluated on the basis of a collection of ~60 international reference materials (Bologne & Duchesne, 1991). We report only the P_2O_5 concentrations in this contribution: the rest of the data will be presented in further publications.

RESULTS

Drill core 90-22; centre of intrusion

In drill core 90-22, the base of UZa occurs at 930 m depth. The transition from a symplectite-dominated late-stage assemblage to one containing granophyre and ilmenite-rich intergrowths begins at 563 m depth [2404 m stratigraphic height according to the scheme of Holness *et al.* (2007*b*)] with the appearance of quartz pockets (e.g. Fig. 7c) coexisting with reactive symplectites (Fig. 5). Reactive symplectites disappear at about 460 m depth, where the stratigraphically lowest interstitial granophyre is observed (Fig. 5). Granophyre (and the associated ilmenite-rich intergrowths) is common at 361 m and increases in abundance upwards.

The stratigraphic variation of Θ_{cpp} in the vicinity of the UZa–b boundary in the 90-22 drill core was presented by Holness (2015) and these data are shown in

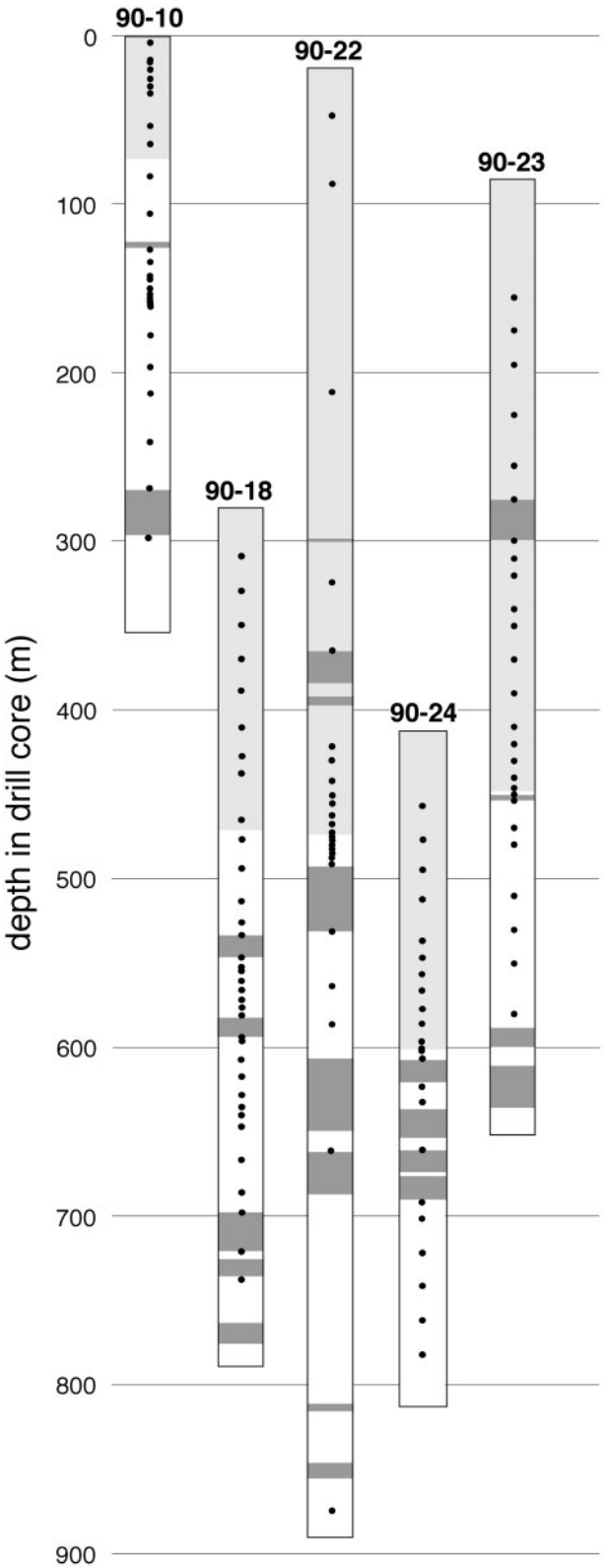

Fig. 9. Logs of the five drill cores, with vertical dimensions given in metres depth in the core (i.e. the zero point on the *y*-axis is the ground surface). Pale grey denotes UZb; white denotes UZa. Late-stage dykes (undifferentiated between granophyre and basalt) are shown as dark grey horizontal bands. The positions of the samples for which we report dihedral angles are shown as black dots.

Fig. 5a. Noteworthy features are the macro-dolerite zone immediately below apatite-in and the narrow stratigraphic range of the positive excursion associated with the arrival of cumulus apatite. This excursion is defined by an increase of Θ_{cpp} that begins at ~481 m and reaches a maximum at ~475 m.

The arrival of cumulus apatite is recorded in a series of closely spaced samples (located at 477·6, 477·1, 476·5, 475·9, 475·5, 474·96, and 471·8 m depth). The stratigraphically lowest sample with apatite primocrysts is at 475·9 m, in which abundant apatite grains form clusters either on boundaries between larger primocrysts of plagioclase, pyroxene or oxides, or within planar-sided triangular interserts containing late-stage magmatic hydrous fine-grained intergrowths (Fig. 10a). Some 50 cm higher in the stratigraphy (at 474·96 m), apatite primocrysts are more homogeneously distributed and not associated particularly with late-stage hydrous intergrowths (Fig. 10b).

Bulk-rock P_2O_5 concentrations in core 90-22 have previously been reported by Tegner *et al.* (2009); these data are shown in Fig. 5b for samples from 600 to 310 m depth. The sample spacing of the bulk compositional analyses is

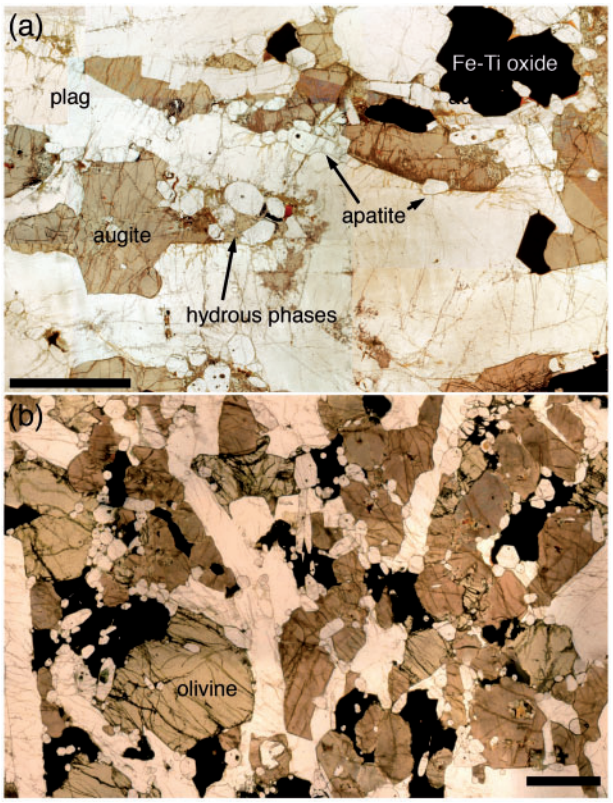

Fig. 10. (a) Photomicrograph of gabbro at 475·9 m depth in drill core 90-22: this is the lowest sample from 90-22 that contains abundant euhedral apatite grains. It should be noted how the apatite grains cluster in triangular spaces between plagioclase primocrysts, and are associated with late-stage, primary magmatic, hydrous minerals. Scale bar represents 2 mm. (b) Gabbro at 471·9 m depth in drill core 90-22. Here the apatite grains are more homogeneously distributed and are no longer clustered within spaces between primocrysts. Scale bar represents 2 mm.

greater than that of the dihedral angle measurements, but within these limitations, the increase in P_2O_5 is simultaneous with the positive excursion in Θ_{cpp} (Fig. 5b)—it should be noted that the sample at 481·8 m depth contains significantly more P_2O_5 (0·23 wt %) than the underlying samples (0·025–0·11 wt %), perhaps indicative of a zone of finite width over which P_2O_5 increases.

Drill core 90-24; centre of intrusion

In drill core 90-24, the base of UZa is at 960 m depth. The transition from a symplectite-dominated late-stage assemblage to one containing granophyre and ilmenite-rich intergrowths is not complete in the section of core examined here, but begins at ~633 m with the appearance of quartz pockets coexisting with reactive symplectites (Fig. 11). Reactive symplectites are present in all samples examined but become rare towards the top of the sample traverse. The stratigraphically lowest interstitial granophyre is observed at ~490 m (Fig. 11).

In the lower parts of this core Θ_{cpp} is constant at 96–97° until about 700 m depth, where it decreases to 84° over a distance of 100 m, forming a zone of macro-dolerite (Fig. 11a) that is intersected by multiple later dykes. An increase to ~100° occurs between 602 and 603 m. Angles fall over ~50 m of stratigraphy to 80–83°, corresponding to the macro-dolerite microstructure in the upper part of the core.

The first appearance of apatite primocrysts occurs between 602 and 603 m depth, corresponding, within the limitiations of our ~1 m sample spacing, to the stepwise increase in Θ_{cpp}. Apatite primocrysts are abundant in the sample at 602 m, in which they are distributed homogeneously. The bulk-rock P_2O_5 concentration in 90-24 is uniformly low (<0·06 wt %) in all samples below 603 m depth, with a stepwise jump to values generally >2·0 wt % in all samples at or above 603 m depth in the core (Fig. 11b).

Drill core 90-18; centre of intrusion

Reactive symplectites are common in the lowest samples examined, and are present until ~400 m depth. The stratigraphically lowest sample in which pockets of

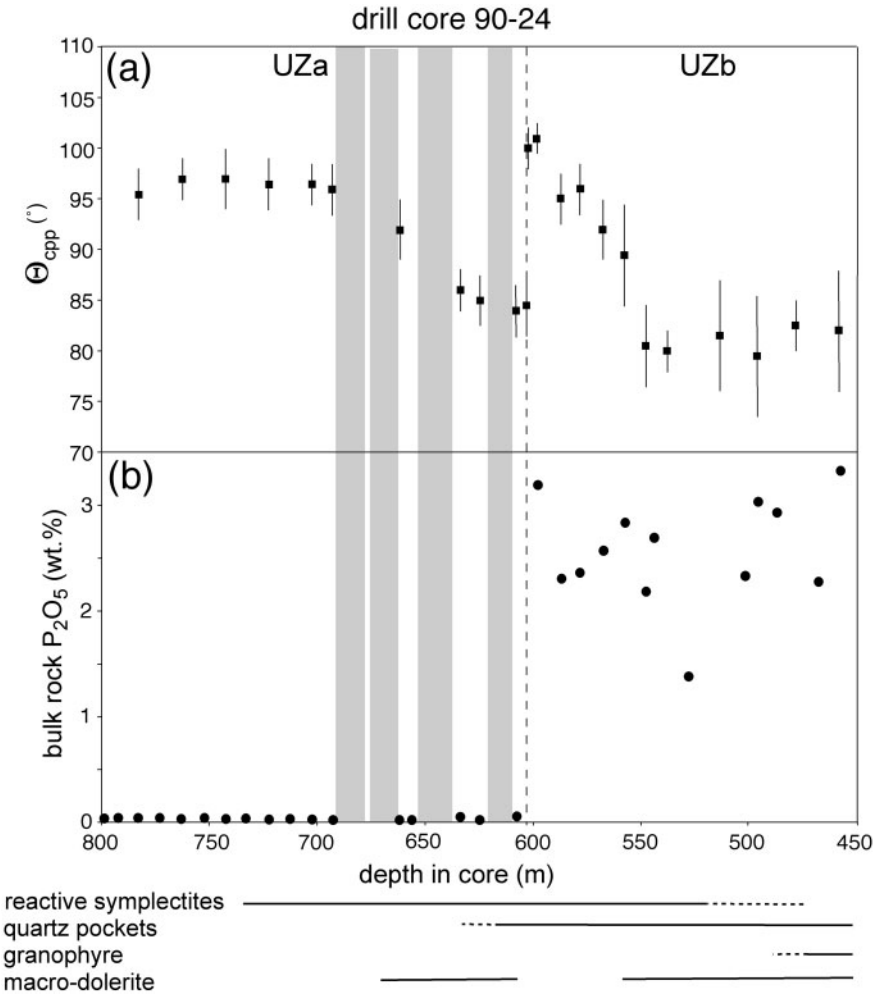

Fig. 11. (a) Variation of Θ_{cpp} in drill core 90-24. The arrival of cumulus apatite is shown as the dotted line at 602·5 m depth in core. The vertical grey bands show the stratigraphic position and extent of late-stage dykes (no distinction is made between mafic and granophyric dykes). (b) The variation of bulk-rock P_2O_5. The continuous lines beneath the graph denote regions of the stratigraphy characterized by different late-stage features, whereas the dotted ends to these lines denote stratigraphic regions where each late-stage feature is present but rare.

quartz, bounded by irregular walls of plagioclase, are observed is at 607 m. K-feldspar, in granophyre, is present at ~550 m depth: the transition between reactive symplectites and paired intergrowths therefore occurs over ~200 m of stratigraphy in this core (Fig. 12).

Θ_{cpp} in this core is constant at 96–99° until about 650 m, where it decreases to 82° over a distance of 50 m, forming a zone of macro-dolerite (Fig. 12a). It then increases to 100–102° and remains in this range for 20 m of stratigraphy (570–550 m) before falling, over a stratigraphic distance of 30 m, to a plateau at 91–93°. Values then fall to 80–85° in the upper parts of the core.

The first appearance of abundant apatite occurs between samples at 476·6 m and 465·1 m depth, where it is fine-grained (0·1 mm diameter) and forms clusters on grain boundaries between other primocryst phases. Apatite grain size increases to 0·3 mm with height, and the grains become more homogeneously distributed.

At stratigraphic levels below that of the arrival of apatite primocrysts, the bulk-rock concentration of P_2O_5 is 0·04–0·07 wt % until about 610 m when it gradually increases to 0·08–0·14 wt % (Fig. 12b and c). At the onset of apatite primocryst growth at 476–457 m, P_2O_5 concentration reaches exceeds 2·5 wt %.

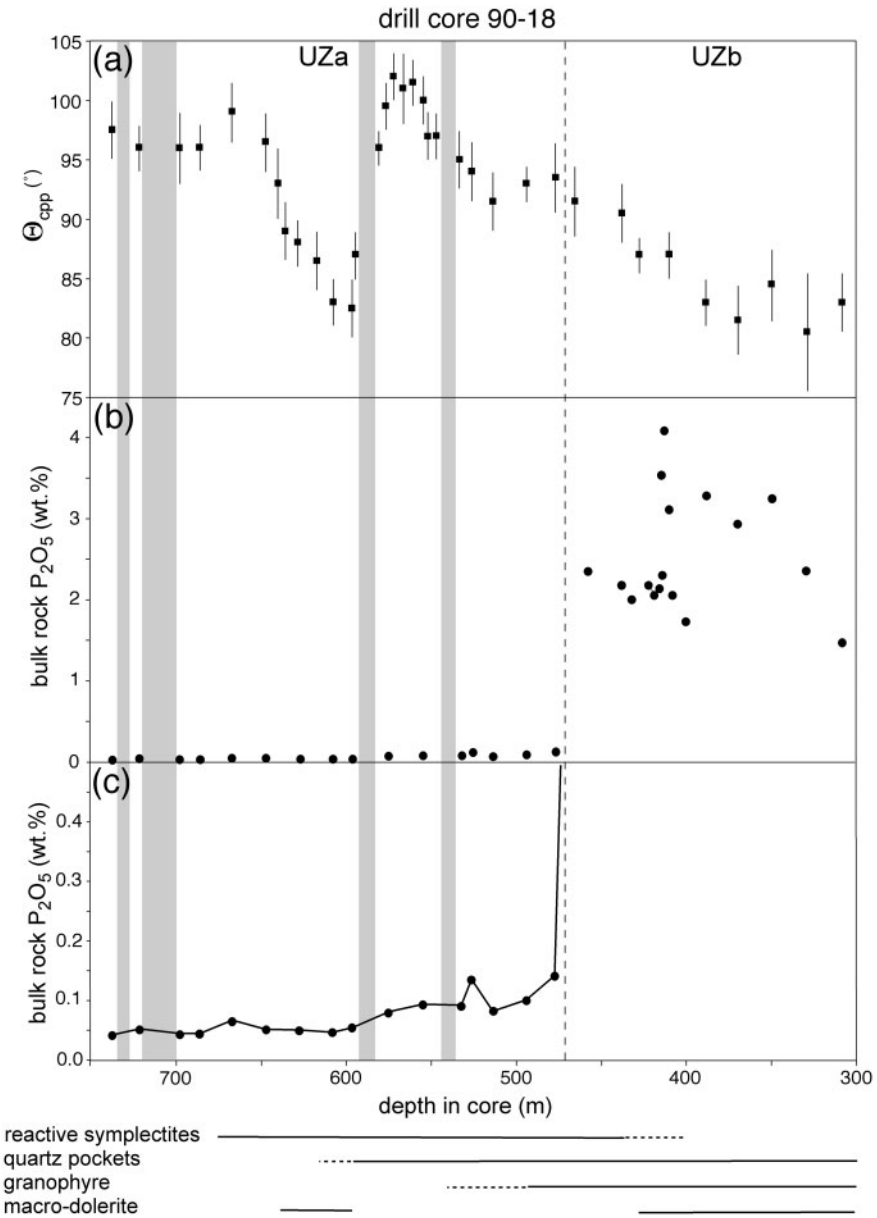

Fig. 12. (a) Variation of Θ_{cpp} in drill core 90-18. The arrival of cumulus apatite is shown as the dotted line at 475 m depth in core. The vertical grey bands show the stratigraphic position and extent of late-stage dykes (no distinction is made between mafic and granophyric dykes). (b) The variation of bulk-rock P_2O_5, with a magnified view of the same data in (c). The stepwise increase in P_2O_5 at ~580 m, coinciding with the region of elevated Θ_{cpp}, should be noted. The continuous lines beneath the graph denote regions of the stratigraphy characterized by different late-stage features, whereas the dotted ends to these lines denote stratigraphic regions where each late-stage feature is rare.

Drill core 90-10; western margin

The base of UZa is recorded at 350 m depth in core 90-10 (Fig. 13). Reactive symplectites are present below ~500 m, but are absent from all overlying samples. Scattered pockets of interstitial quartz, bounded by irregular plagioclase walls, are present at 491 m, with the lowest appearance of granophyre at 300 m. Granophyre and associated ilmenite-rich intergrowths are abundant from ~200 m.

Dihedral angles were measured in the upper 270 m of this core (Fig. 13a). Θ_{cpp} is constant at 96–99° between 270 m and 160 m where it increases over 3 m to a maximum of 105 ± 3°. It remains in the range 101–105° until 144 m where it declines over 20 m to a plateau at 96–97°. Between 34 m and 20 m Θ_{cpp} declines to a minimum of 87 ± 3·5° before climbing back to 98 ± 4·5° in the shallowest 20 m of the core.

The stratigraphically lowest appearance of abundant apatite primocrysts is between the two samples at 73·9 m and 64·2 m depth. In sample 64·2 m clusters of ~0·1 mm diameter grains are present at the margins of other primocrysts and within planar-sided pockets of granophyre. The grain size increases upwards, reaching a final value of 0·3–0·5 mm diameter by 34·1 m depth. At this level apatite is homogeneously distributed.

Below 105 m, the bulk-rock P_2O_5 concentration is in the range 0·06–0·17 wt % (Fig. 13b). Between 105 m and 95 m depth this begins to increase, reaching 1 wt % at 73·9 m and ~2·5 wt % by 64 m. There is a localized excursion to 3·5 wt % at 16 m.

Drill core 90-23; eastern margin

The base of UZa occurs at 720 m depth in core 90-23, although we did not examine the lower part of the core in detail. There are no reactive symplectites above ~500 m. Instead, granophyre is abundant, filling pockets predominantly bounded by planar-sided plagioclase grains. Some ilmenite-rich intergrowths are also present.

Θ_{cpp} is constant through UZa, in the range 93–94°, with an increase to 101° ± 2·5° in the sample at 450·39 m, coinciding (at the resolution of the sample spacing) with the first appearance of abundant apatite (Fig. 14). Θ_{cpp} then declines smoothly over a distance of

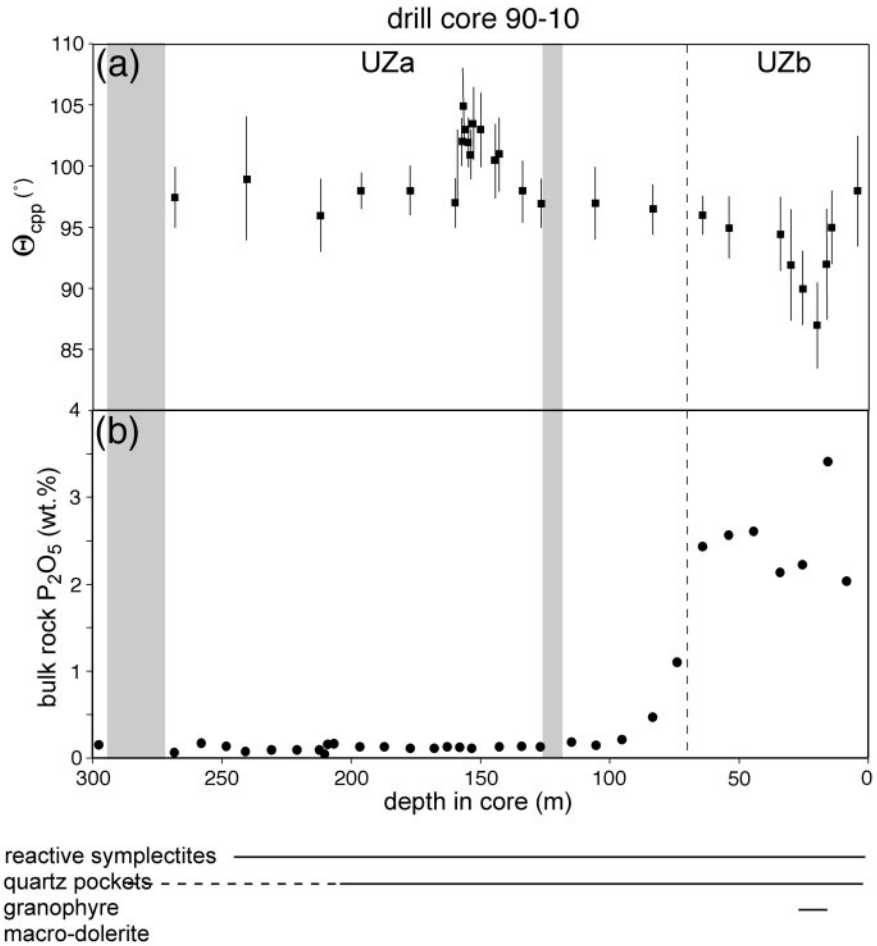

Fig. 13. (a) Variation of Θ_{cpp} in drill core 90-10. The arrival of cumulus apatite is shown as the dotted line at 65 m depth in core. The vertical grey bands show the stratigraphic position and extent of late-stage dykes (no distinction is made between mafic and granophyric dykes). (b) The variation of bulk-rock P_2O_5. The continuous lines beneath the graph denote regions of the stratigraphy characterized by different late-stage features, whereas the dotted ends to these lines denote stratigraphic regions where each late-stage feature is rare.

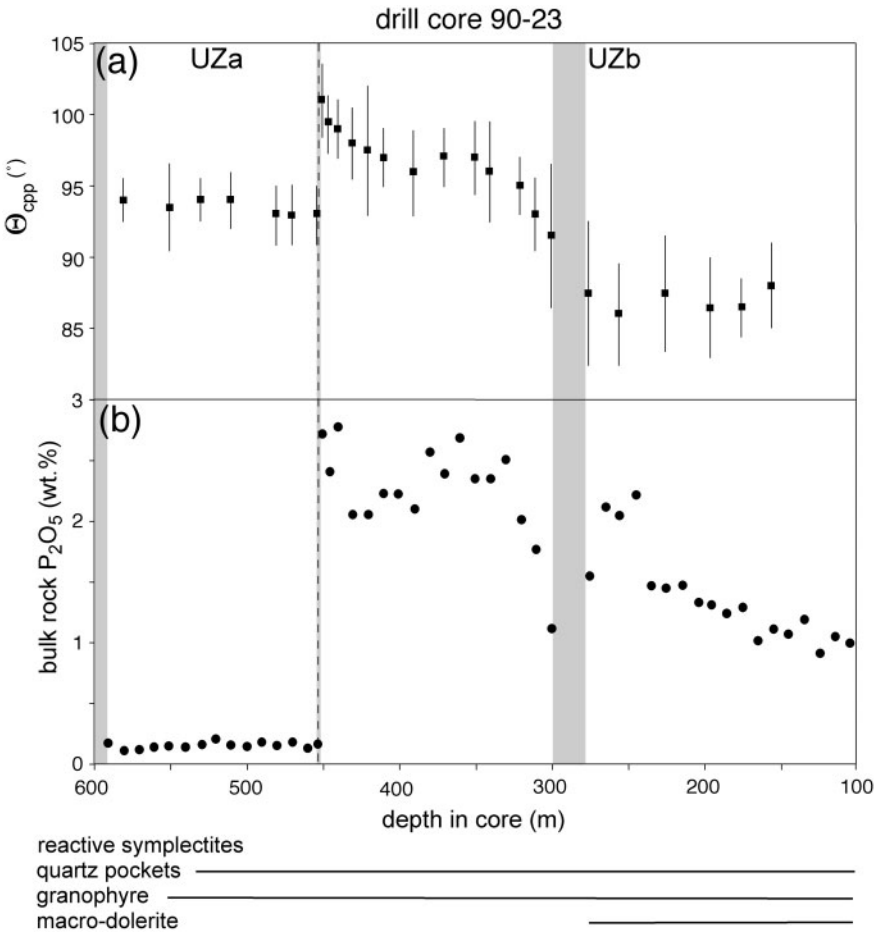

Fig. 14. (a) Variation of Θ_{cpp} in drill core 90-23. The arrival of cumulus apatite is shown as the dotted line at 455 m depth in core. The vertical grey bands show the stratigraphic position and extent of late-stage dykes (no distinction is made between mafic and granophyric dykes). (b) The variation of bulk-rock P_2O_5. The continuous lines beneath the graph denote regions of the stratigraphy characterized by different late-stage features, whereas the dotted ends to these lines denote stratigraphic regions where each late-stage feature is rare.

40 m to a plateau at 96–97°. At ~330 m depth Θ_{cpp} begins a smooth upwards decrease over about 70 m to 86–88°.

The grain size of the apatite increases upwards, from ~0·1 mm diameter in the deepest sample containing abundant apatite crystals (450·39 m), to 0·3–0·6 mm diameter at 410·34 m. In UZa, the bulk-rock P_2O_5 concentration is 0·1–0·22 wt % (Fig. 14b). Between the two analyses at 454 m and 450·9 m it increases to 2·7 wt %. The bulk concentration then shows an irregular but steady decline, with many localized excursions from the general trend until 235 m where any departures from the trend are much smaller.

THE AMOUNT OF TRAPPED LIQUID

P is an incompatible element below UZb, so, using the method of Tegner *et al.* (2009), the concentration of P_2O_5 can be used to estimate the amount of liquid in the crystal mush at the moment it became saturated in apatite. This estimate is a minimum, however, in rocks in which the interstitial liquid split into two immiscible conjugates. P_2O_5 is preferentially partitioned into the Fe-rich conjugate (Charlier & Grove, 2012), so if the retained liquid is dominated by the Fe-rich conjugate (owing to preferential loss of its Si-rich counterpart), the bulk-rock P_2O_5 concentrations of the fully solidified cumulate will be higher than expected. In cumulates containing abundant reactive symplectites, such calculations may therefore over-estimate the amount of remaining intercumulus liquid.

We calculated the fraction of trapped liquid in UZa of each of the drill cores by dividing the bulk phosphorus content of each sample by the phosphorus content in the model liquid of Tegner *et al.* (2009). Because progressive fractionation acts to increase phosphorus in the bulk liquid, the appropriate liquid composition is dependent on the relative stratigraphic position of each sample. This position was calculated by establishing a relative height within UZa (base = 0, top = 1) in all cores. The compositional data from 90-22 from Tegner *et al.* (2009) was used to establish a polynomial relationship between relative stratigraphic height and the phosphorus content of the liquid, and therefore to calculate the fraction of trapped liquid in the remaining three cores. The results are shown in Fig. 15.

Whereas the amount of trapped liquid in cores 90-22 and 90-24 is estimated to be relatively constant at 4–5 wt % (e.g. Tegner *et al.*, 2009), that in cores 90-10 and 90-23 is highly variable, ranging from 5 to 25 wt %, with average values of the order of 10 wt %. The lower part of UZa sampled by drill core 90-18 contains estimated volumes of trapped liquid comparable with that in cores 90-22 and 90-24, but from 575 m depth the volume of liquid progressively increases to values similar to those in 90-10 and 90-23 by the top of UZa (Fig. 15). The stratigraphic height of the increase in calculated trapped liquid corresponds to the region of elevated Θ_{cpp} (Fig. 12c). Because this region of core 90-18 is characterized by reactive symplectites, the actual volume of liquid present in the mush may have been higher than in our calculations.

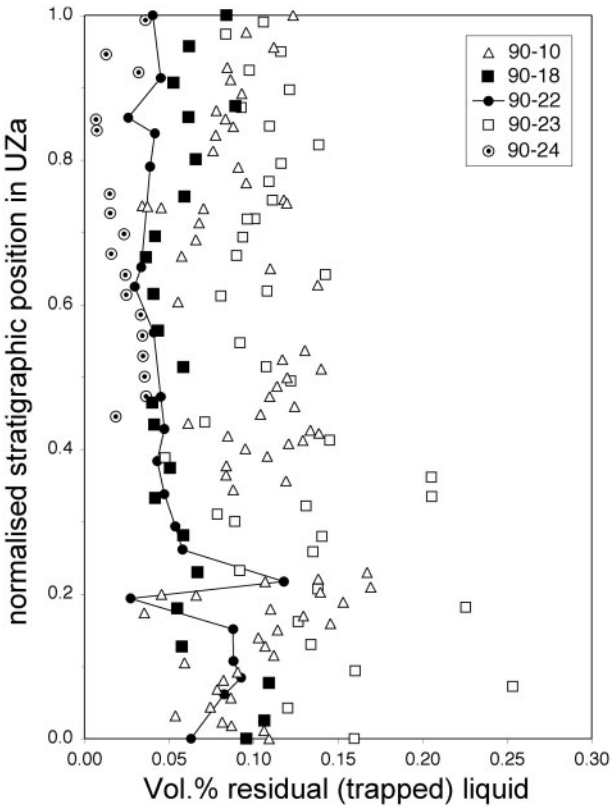

Fig. 15. Trapped liquid fraction in the five drill cores as a function of normalized height within UZa, calculated according to the method of Tegner *et al.* (2009). (See text for details.)

DISCUSSION

Comparison between the five cores: defining critical features of interest

Because the bulk magma is likely to have been well mixed (Salmonsen & Tegner, 2013), the appearance of cumulus apatite at the magma–mush interface occurred at the same time everywhere on the floor: the five cores can therefore be correlated using the first appearance of cumulus apatite. Because we are interested in the true stratigraphic variation of dihedral angles, which are likely to be formed at different depths and different times in the mushy layer sampled by each core, we correlated the variation of Θ_{cpp} in the cores by removing all dykes thicker than a few metres, shifting up all samples below apatite-in and shifting down all samples above apatite-in, using apatite-in as the zero point marker for each core (Fig. 16).

Decoding (and predicting) the absolute value of Θ_{cpp} still represents a significant challenge, given the stochastic nature of three-grain junction formation by randomly impinging plagioclase grains. In contrast, the relative variation of Θ_{cpp}, and its relationship with parameters such as the offset between the spike and the appearance of cumulus apatite, the bulk-rock P_2O_5 concentration, and the grain size and distribution of apatite, can be usefully interpreted to create a snapshot of the porosity profile through the mush on the chamber floor in UZ at the UZa–UZb boundary.

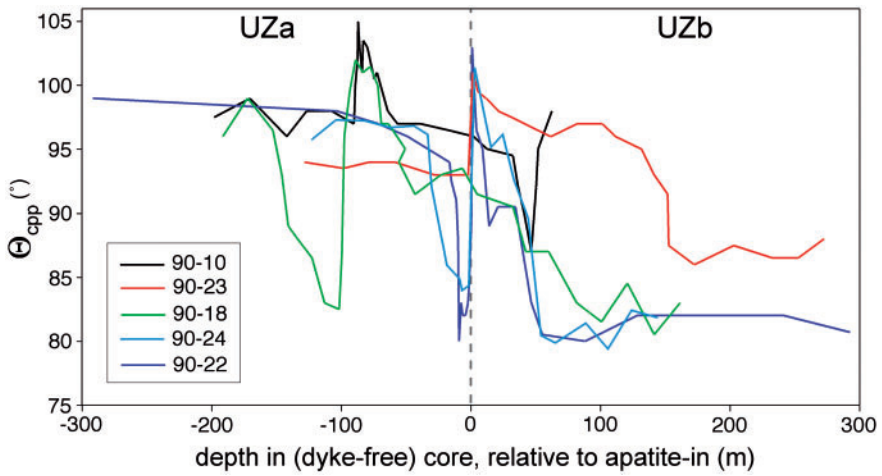

Fig. 16. The variation of Θ_{cpp} in the five drill cores. For each core the stratigraphic position of the samples is adjusted by the removal of the dykes so that the sections of gabbro are continuous and uninterrupted. To allow comparison between the cores, the zero point of the stratigraphy is placed at the first arrival of cumulus apatite.

In general, the underlying patterns of Θ_{cpp} variation are similar in the five cores, with well-defined, spike-like excursions, followed by a plateau and a drop to much lower angles. The stratigraphic height, relative to apatite-in, of the upper macro-dolerite zone is the same in 90-10, 90-18, 90-22 and 90-24. In detail, however, there are significant differences: three of the five cores contain regions of low Θ_{cpp} (macro-dolerite) below apatite-in; the zone of high Θ_{cpp} associated with the arrival of cumulus apatite is a sharply defined spike in 90-22 and 90-24, but forms a broad plateau over some tens of metres in 90-10 and 90-18; there is also a significant stratigraphic separation between the Θ_{cpp} spike and the appearance of cumulus apatite in 90-10 and 90-18. Finally, Θ_{cpp} is very different in 90-23, with comparatively low values in UZa and high values in UZb, and a stratigraphically higher arrival of the macro-dolerite microstructure in UZb, compared with the other cores.

Linking microstructure and P_2O_5 concentrations

The observed stratigraphic variations in bulk-rock P_2O_5 concentration and microstructure form two clearly defined groups of microstructural and geochemical characteristics. The first group, seen in the two marginal cores 90-10 and 90-23, comprises elevated (>0·1 wt %) bulk-rock P_2O_5 concentrations throughout UZa, a stratigraphically low transition (e.g. in MZ) from reactive symplectites to paired intergrowths and an absence of macro-dolerite below apatite-in. The second group comprises generally low (<0·1 wt %) bulk-rock P_2O_5 concentrations in UZa, a stratigraphically high transition to paired intergrowths (e.g. in UZ) and macro-dolerite below apatite-in: this is found in the three central cores, 90-18, 90-22 and 90-24. These two groups can be interpreted in terms of the behaviour of the interstitial liquid.

An elevated bulk-rock P_2O_5 concentration below UZb is generally interpreted as evidence of abundant retained liquid (e.g. Tegner *et al.*, 2009). Similarly, a stratigraphically low transition from reactive symplectites to paired intergrowths has been interpreted as the record of generally ineffective expulsion of the interstitial liquid, leading to retention of the Si-rich conjugate low in the stratigraphy (Holness *et al.*, 2011). Because these two characteristics are associated with the absence of macro-dolerite in UZa, it suggests that this too is indicative of a generally high volume of retained interstitial liquid. We conclude that the two drill cores from the margins of the intrusion (90-10 and 90-23) retained significantly more interstitial liquid than did the three central cores [see Nielsen *et al.* (2015), who came to the same conclusion on the basis of lateral variations in the PGE–Au mineralization in MZ].

The record of mush thickness

As a simple and generalized first approximation, we can use the relationship between AR and crystallization time of Holness (2014) to estimate mush thickness on the Skaergaard chamber floor. Estimates of the solidification time for the 3 km of cumulate stratigraphy of the Skaergaard Intrusion are of the order of 300 000 years (Larsen & Tegner, 2006), leading to an average time of 100 years to create 1 m of floor cumulate; these values are comparable to the 1–4 cm a^{-1} accumulation rate suggested by Morse (2011) and the 2 cm a^{-1} suggested by Irvine (1970) for LZc and MZ. The solidification rate is likely to have been at the lower bound of 1 cm a^{-1} of Morse (2011) in UZ, where AR is ~2·0 in drill core 90-22 (Holness, 2015; Fig. 4a). By comparison with sills, plagioclase grains of this shape are formed when the crystallization time is ~800 years (Holness, 2014), translating into a mushy layer thickness of 8 m in the centre of the floor. In the lower parts of the Layered Series, sampled on the Uttental Plateau (Fig. 2), AR is 3–3·5 (Holness, 2015; Fig. 4a), corresponding to 1–10 years crystallization time (Holness, 2014). Assuming an accumulation rate of 4 cm a^{-1} (Morse, 2011), this translates into a mush layer 4–40 cm thick. Although these numbers are approximate, and are based on the assumption of *in situ* growth with no contribution from the deposition of grains grown in the rapidly cooling environment of the walls, they support a thin (<10 m) mushy layer.

Another simple estimate of mush thickness can be determined using the range of dihedral angles in the Skaergaard Layered Series. The range of 85–100° (Fig. 4b) is equivalent (at least in essentially unfractionated sills) to crystallization times of 30–1000 years, leading to an estimated mush thickness of 120 cm to 10 m [using the range of accumulation rates of 1–4 cm a^{-1} of Morse (2011)].

More specific indications of mush thickness can be obtained from a consideration of the stratigraphic distance between the Θ_{cpp} excursion related to the arrival of liquidus apatite and the first appearance of cumulus apatite, together with the stratigraphic variation of bulk-rock P_2O_5 concentration. The significant offsets of these two features observed in cores 90-10 and 90-18 are associated with an extended Θ_{cpp} excursion and a gradual increase in bulk-rock P_2O_5 concentration at the UZa–b boundary. In core 90-10, the Θ_{cpp} peak occurs 90 m below the first appearance of abundant apatite, and the first appearance of large, homogeneously distributed, apatite grains is yet another 30 m higher in the stratigraphy. These observations are consistent with an extended thickness of highly porous mush and an overall thickness of the mushy layer of >100 m. The microstructural and geochemical data point to a similar mush thickness in 90-18. Conversely, in the other three cores (90-22, 90-23, 90-24) the step-change in Θ_{cpp} either coincides with (at least within the limitations of our sample spacing), or is offset by only a few metres from, the first petrographic appearance of cumulus apatite: in these cores the positive Θ_{cpp} excursion is narrow and there is a sharp increase in bulk P_2O_5 at the UZa–b boundary. We therefore deduce that the mushy layer was thin (<5 m) in these three cores.

It should be noted that this method of deducing mush thickness underestimates the distance from the top of the mush to the horizon where solidification is complete

in rocks with elevated bulk-rock P_2O_5 concentrations in UZa (cores 90-10 and 90-23), but provides a better estimate for those with generally low bulk-rock P_2O_5 in UZa (cores 90-22 and 90-24, and the lower parts of 90-18).

These deductions are consistent with the shape of the Θ_{cpp} excursion associated with the arrival of cumulus apatite. The change in cooling rate owing to these transient variations in the contribution of latent heat to the enthalpy budget (fractional latent heat) is transferred downwards from the magma–mush interface to the base of the mushy layer by thermal diffusion. The thermal time constant for a 150 m thick layer with a thermal diffusivity of 10^{-6} m^2 s^{-1} is of the order of 75 years, whereas an average rate of upwards migration of the magma–mush interface is 300 years per metre. A thermal signal could thus penetrate to the base of a mushy layer 150 m thick on a much faster time-scale than the overall solidification rate. However, this signal will broaden as it diffuses downwards, leading to a broad zone of high angles over a significant portion of the stratigraphy in cumulates that crystallized from a thick mushy layer, but a spike-like excursion in cumulates that crystallized from a thin mushy layer. The Θ_{cpp} excursion is spike-like in 90-22, 90-24 and, to a lesser extent, in 90-23. In contrast, Θ_{cpp} is $>100^\circ$ over some tens of metres of stratigraphy in 90-18 and, although the Θ_{cpp} excursion in 90-10 is not quite as broad, it is wider than those observed in 90-22 and 90-24.

Implications for models of adcumulate formation

The combined microstructural and compositional data suggest that the efficiency of expulsion of evolved interstitial liquid was greatest at the centre of the intrusion floor and least near the walls, and the mushy layer on the floor, at the moment of saturation of the bulk liquid in apatite, is represented by <5 m of fully solidified cumulates at the centre and at the eastern margin (three cores) but by $\sim$100 m of fully solidified cumulates near the western margin (two cores). There is no correlation between the efficiency of expulsion of evolved interstitial liquid and the mushy layer thickness: the least efficient expulsion occurred near the margins of the floor, in a mushy layer that was at least 100 m thick in the west but only a few metres thick in the east. Conversely, the most efficient liquid expulsion occurred in the centre of the floor in one place where the mushy layer was $\sim$100 m thick and in two others where it was only a few metres thick.

Most models describing the behaviour of late-stage evolved interstitial liquids are dependent on mushy layer thickness. Both the compaction model (Sparks *et al.*, 1985; McKenzie, 2011), and those based on compositional convection (Sparks *et al.*, 1985; Tait & Jaupart, 1992) predict a positive correlation between mush thickness and the effectiveness of expulsion of evolved liquids and the extent to which the resultant cumulates reach the adcumulate endmember. Conversely, a negative correlation is required to support the suggestion of Wager *et al.* (1960) that adcumulates form under conditions of effective diffusive mass transport in the mush. The absence of any such correlation in UZa therefore suggests that none of these models adequately describe the behaviour of evolved interstitial liquids in Skaergaard. That compaction was not a significant process in Skaergaard, at least in that part of the stratigraphy near the UZa–b boundary, is also suggested by the near-constant stratigraphic thickness of the Triple Group across the entire floor of the intrusion (Nielsen *et al.*, 2015).

It should be noted, however, that we have derived the thickness of the mush only at the moment the bulk magma became saturated in apatite: it is possible that the thicknesses we observe were temporary. Features such as localized tearing, faulting, slumping and cross-bedding (Wager & Deer, 1939; McBirney & Nicolas, 1997; Humphreys & Holness, 2010), together with compositional discontinuities (Hoover, 1989; Nielsen *et al.*, 2015), point to erosion of the crystal mush forming on the vertical chamber walls. Mineral lineations point away from the western wall, towards a focus in the region of the collar for 90-18 (McBirney & Nicolas, 1997). The outermost regions of the Layered Series are relatively rich in Fe–Ti oxides, suggestive of addition of these heavy mineral grains from an eroding, physically unstable, mushy layer on the walls (Wager & Brown, 1968). It is therefore possible that the greater thickness of the floor mush recorded at the UZa–b boundary on the western margins of the floor was a temporary feature caused by localized wall collapse.

Conversely, the thinner mush on the central and eastern parts of the floor may also have been a transient phenomenon caused by convective scouring of the floor with a predominant east-to-west current direction. The cooling of the intrusion is likely to have been asymmetric late in the solidification history, when the hydrothermal circulation system was active and concentrated in the fractured overlying plateau lavas in the east. The magma chamber may also have been asymmetric: Nielsen (2004) suggested that MZ may be thinner in the east, pointing to contemporaneous tilting of the intrusion and therefore a westwards-dipping roof. Such a geometry might have contributed to a preferred westward circulation system and temporary displacement of poorly consolidated mush from east to west.

The stratigraphic distribution of the macro-dolerite microstructure

The macro-dolerite microstructure of UZb is a consequence of plagioclase no longer being a volumetrically important phase in the assemblage crystallizing from the last liquids, resulting in no overgrowth of primocrysts. The three cores with the macro-dolerite microstructure in UZa are those that contained little interstitial liquid (90-18, 90-22 and 90-24). The early development of macro-dolerite seems, therefore, to be controlled by the amount of interstitial liquid retained in the cumulate pile. We suggest that the stratigraphically

lower development of macro-dolerite in these three cores compared with 90-10 and 90-23 (in which macro-dolerite is seen only in UZb) is because the last drops of liquid remaining in mush from which interstitial liquid is efficiently expelled will generally be very highly evolved as a consequence of extended *in situ* crystallization.

Θ_{cpp}, and therefore the amount of late-stage plagioclase growth, increases markedly in 90-18, 90-22 and 90-24 when the bulk liquid becomes saturated in apatite. An expected consequence of the addition of a phase to the liquidus assemblage is an increase in crystal productivity (Ghiorso, 1997; Holness *et al.*, 2007*a*; Morse, 2011). It is possible that this would lead to a decreased permeability of the mushy layer and thus an increase in the amount of interstitial liquid. Such an effect is observed in 90-18, in which the bulk-rock P_2O_5 concentration doubles immediately below the apatite-in Θ_{cpp} step-change (Fig. 12). An increase in the amount of interstitial liquid would result in a less evolved average composition of the liquid from which clinopyroxene–plagioclase–plagioclase junctions form and therefore permit plagioclase crystallization at the three-grain junctions. This is effective over only a limited stratigraphic range, as the composition of the bulk liquid in the magma chamber, and hence the composition of the liquid in the mush, becomes increasingly evolved with stratigraphic height, eventually resulting in the resumption of macro-dolerite formation.

The high values of Θ_{cpp} observed in the topmost few metres of core 90-10 are puzzling. These samples contain abundant mafic minerals and oxides, with little plagioclase. We suggest that the late-stage liquids in these Fe-rich rocks were not particularly granophyric and therefore that plagioclase could crystallize during the formation of the clinopyroxene–plagioclase–plagioclase three-grain junctions.

CONCLUSIONS

Microstructures preserved in the UZ gabbros of the Skaergaard Layered Series are consistent with significant differences in the thickness of the mushy layer across the magma chamber floor at the moment when the bulk magma became saturated in apatite. The floor mush was ~100 m thick at the western margin, but only a few metres thick in the centre and at the east. There is no correlation between mush thickness and the efficiency of expulsion of evolved interstitial liquid, suggesting that the extent of adcumulus crystallization in the floor cumulates was not controlled by processes dependent on mush thickness. However, it is possible that the absence of any correlation is because the microstructures are recording a transient episode of either scouring or deposition near the UZa–b boundary.

ACKNOWLEDGEMENTS

We thank Charles E. Lesher, Peter Thy, Llewellyn Pilbeam, Søren Roested Madsen and Madeleine Humphreys for assistance in sampling the drill cores. An earlier version of this contribution was significantly improved following the helpful comments of James Mungall, Alan Boudreau, Chris Lee and an anonymous reviewer.

FUNDING

M.B.H. and C.T. acknowledge support from a Royal Society Joint International Grant. M.B.H. was supported by the Natural Environment Research Council (grant numbers NE/F020325/1 and NE/J021520/1). C.T. was supported by the Carlsberg Foundation, the Danish Council of Independent Research, and the Danish National Research Foundation.

SUPPLEMENTARY DATA

Supplementary data for this paper are available at *Journal of Petrology* online.

REFERENCES

Andersen, J. C. Ø., Rasmussen, H., Nielsen, T. F. D. & Ronsbø, J. G. (1998). The Triple Group and the Platinova gold and palladium reefs in the Skaergaard intrusion: Stratigraphic and petrographic relations. *Economic Geology and the Bulletin of the Society of Economic Geologists* **93**, 488–509.

Bird, D. K., Rogers, R. D. & Manning, C. E. (1986). Mineralized fracture systems of the Skaergaard intrusion, East Greenland. *Meddelelser om Grønland, Geoscience* **16**, 1–65.

Bird, D. K., Brooks, C. K., Gannicott, R. A. & Turner, P. A. (1991). A gold-bearing horizon in the Skaergaard intrusion, East Greenland. *Economic Geology* **86**, 1083–1092.

Botcharnikov, R. E., Almeev, R. R. & Holtz, F. (2008). Phase relations and liquid lines of descent in hydrous ferrobasalt—implications for the Skaergaard intrusion and Columbia River basalts. *Journal of Petrology* **49**, 1687–1727.

Bologne, G. & Duchesne, J. C. (1991). Analyse des roches silicatées par spectrométrie de fluorescence X: précision et exactitude. *Professional Paper, Geological Survey of Belgium* **249**, 11 pp.

Boorman, S., Boudreau, A. & Kruger, F. J. (2004). The Lower Zone–Critical Zone transition of the Bushveld Complex: A quantitative textural study. *Journal of Petrology* **45**, 1209–1235.

Boudreau, A. E. & McCallum, I. S. (1992). Concentration of platinum-group elements by magmatic fluids in layered intrusions. *Economic Geology* **87**, 1830–1848.

Boudreau, A. E. & Meurer, W. P. (1999). Chromatographic separation of the platinum-group elements, gold, base metals and sulfur during degassing of a compacting and solidifying igneous crystal pile. *Contributions to Mineralogy and Petrology* **134**, 174–185.

Brooks, C. K. & Nielsen, T. F. D. (1978). Early stages in the differentiation of the Skaergaard magma as revealed by a closely related suite of dyke rocks. *Lithos*, **11**, 1–14.

Brown, P. E., Chambers, A. D. & Becker, S. M. (1987). A large soft-sediment fold in the Lilloise Intrusion. In: Parsons, I. (ed.) *Origins of Igneous Layering*. East Greenland: Springer, pp. 125–143.

Bufe, N. A., Holness, M. B. & Humphreys, M. C. S. (2014). Contact metamorphism of Precambrian gneiss by the Skaergaard Intrusion. *Journal of Petrology* **55**, 1595–1617.

Butcher, A. R., Young, I. M. & Faithfull, J. W. (1985). Finger structures in the Rhum Complex. *Geological Magazine* **122**, 491–502.

Chambers, A. D. & Brown, P. E. (1995). The Lilloise Intrusion, East Greenland: fractionation of a hydrous alkali picritic magma. *Journal of Petrology* **36**, 932–963.

Charlier, B. & Grove, T. L. (2012). Experiments on liquid immiscibility along tholeiitic liquid lines of descent. *Contributions to Mineralogy and Petrology* **164**, 27–44.

Charlier, B., Namur, O., Toplis, M. J., Schiano, P., Cluzel, N., Higgins, M. D. & Vander Auwera, J. (2011). Large-scale silicate liquid immiscibility during differentiation of tholeiitic basalt to granite and the origin of the Daly gap. *Geology* **39**, 907–910.

Cheadle, M. J., Elliott, M. T. & McKenzie, D. (2004). Percolation threshold and permeability of crystallising igneous rocks: the importance of textural equilibrium. *Geology* **32**, 757–760.

Duchêne, S., Pupier, E., Le Carlier De Veslud, C. & Toplis, M. J. (2008). A 3D reconstruction of plagioclase crystals in a synthetic basalt. *American Mineralogist* **93**, 893–901.

Ghiorso, M. S. (1997). Thermodynamic models of igneous processes. *Annual Review of Earth and Planetary Sciences* **25**, 221–241.

Hess, H. H. (1960). Stillwater igneous complex. *Geological Society of America, Memoirs* **80**, 230 pp.

Hess, G. B. (1972). Heat and mass transport during crystallisation of the Stillwater Igneous Complex. In: *Geological Society of America, Memoirs* **132**, 503–520.

Higgins, M. D. (1994). Numerical modelling of crystal shapes in thin sections: estimation of crystal habit and true size. *American Mineralogist* **79**, 113–119.

Holness, M. B. (2010). Decoding dihedral angles in melt-bearing and solidified rocks. *Journal of the Virtual Explorer* **35**, paper 3, doi:10.3809/jvirtex. 2010.00265.

Holness, M. B. (2014). The effect of crystallization time on plagioclase grain shape in dolerites. *Contributions to Mineralogy and Petrology* **168**, 1076, doi:10.1007/s00410-014-1076-5.

Holness, M. B. (2015). Plagioclase growth rates control three-grain junction geometry in dolerites and gabbros. *Journal of Petrology* **56**, 2117–2144.

Holness, M. B. & Winpenny, B. (2009). The Unit 12 allivalite, Eastern Layered Intrusion, Isle of Rum: a textural and geochemical study of an open-system magma chamber. *Geological Magazine* **146**, 437–450.

Holness, M. B., Nielsen, T. F. D. & Tegner, C. (2007a). Textural maturity of cumulates: a record of chamber filling, liquidus assemblage, cooling rate and large-scale convection in mafic layered intrusions. *Journal of Petrology* **48**, 141–157.

Holness, M. B., Tegner, C., Nielsen, T. F. D., Stripp, G. & Morse, S. A. (2007b). A textural record of solidification and cooling in the Skaergaard Intrusion, East Greenland. *Journal of Petrology* **48**, 2359–2377.

Holness, M. B., Morse, S. A. & Tegner, C. (2009). Response to Comment by McBirney, Boudreau and Marsh. *Journal of Petrology* **50**, 97–102.

Holness, M. B., Stripp, G., Humphreys, M. C. S., Veksler, I. V., Nielsen, T. F. D. & Tegner, C. (2011). Silicate liquid immiscibility within the crystal mush: late-stage magmatic microstructures in the Skaergaard Intrusion, East Greenland. *Journal of Petrology* **52**, 175–222.

Holness, M. B., Humphreys, M. C. S., Sides, R., Helz, R. T. & Tegner, C. (2012a). Towards an understanding of disequilibrium dihedral angles in mafic rocks. *Journal of Geophysical Research* doi:10.1029/2011JB008902.

Holness, M. B., Richardson, C. & Helz, R. T. (2012b). Disequilibrium dihedral angles in dolerite sills: a new proxy for cooling rate. *Geology* **40**, 795–798.

Holness, M. B., Namur, O. & Cawthorn, R. G. (2013). Disequilibrium dihedral angles in layered intrusions: a microstructural record of fractionation. *Journal of Petrology* **54**, 2067–2093.

Holness, M. B., Tegner, C., Namur, O. & Pilbeam, L. (2015). The earliest history of the Skaergaard magma chamber: a textural and geochemical study of the Cambridge drill core. *Journal of Petrology* **56**, 1199–1227.

Holwell, D. & Keays, R. R. (2014). The formation of low-volume, high-tenor magmatic PGE–Au sulfide mineralisation in closed systems: evidence from precious and base metal geochemistry of the Platinova reef, Skaergaard Intrusion, East Greenland. *Economic Geology* **109**, 387–406.

Hoover, J. D. (1989). Petrology of the Marginal Border Series of the Skaergaard Intrusion. *Journal of Petrology* **30**, 399–439.

Humphreys, M. C. S. & Holness, M. B. (2010). Melt-rich segregations in the Skaergaard Marginal Border Series: tearing of a vertical silicate mush. *Lithos* **119**, 181–192.

Hunter, R. H. (1996). Texture development in cumulate rocks. In: Cawthorn, R. G. (ed.) *Developments in Petrology*, **15**, Amsterdam: Elsevier, pp. 77–101.

Hunter, R. H. & Sparks, R. S. J. (1987). The differentiation of the Skaergaard intrusion. *Contributions to Mineralogy and Petrology* **95**, 451–461.

Hunter, R. H. & Sparks, R. S. J. (1990). The differentiation of the Skaergaard Intrusion. Reply to McBirney, A. R. & Naslund, H. R. *Contributions to Mineralogy and Petrology* **104**, 248–254.

Irvine, T. N. (1970). Heat transfer during solidification of layered intrusions. I. Sheets and sills. *Canadian Journal of Earth Science* **7**, 1031–1061.

Irvine, T. N. (1980). Magmatic infiltration metasomatism, double-diffusive fractional crystallisation and adcumulus growth in the Muskox intrusion and other layered intrusions. In: Hargraves, R. B. (ed.) *Physics of Magmatic Processes*. Princeton University Press, pp. 325–384.

Irvine, T. N., Andersen, J. C. Ø. & Brooks, C. K. (1998). Included blocks (and blocks within blocks) in the Skaergaard intrusion: geological relations and the origins of rhythmic modally graded layers. *Geological Society of America Bulletin*, **110**, 1398–1447.

Jakobsen, J. K., Tegner, C., Brooks, C. K., Kent, A. J. R., Lesher, C. E., Nielsen, T. F. D. & Wiedenbeck, M. (2010). Parental magma of the Skaergaard intrusion: constraints from melt inclusions in primitive troctolite blocks and FG-1 dykes. *Contributions to Mineralogy and Petrology* **159**, 61–79.

Jang, Y. D., Naslund, H. R. & McBirney, A. R. (2001). The differentiation trend of the Skaergaard intrusion and the timing of magnetite crystallisation: iron enrichment revisited. *Earth and Planetary Science Letters* **189**, 189–196.

Larsen, R. B. & Brooks, C. K. (1994). Origin and evolution of gabbroic pegmatites in the Skaergaard intrusion, East Greenland. *Journal of Petrology* **35**, 1651–1679.

Larsen, R. B. & Tegner, C. (2006). Pressure conditions for the solidification of the Skaergaard intrusion: eruption of East Greenland flood basalts in less than 300,000 years. *Lithos* **92**, 181–197.

Larsen, R. B., Brooks, C. K. & Bird, D. K. (1992). Methane bearing aqueous saline solutions in the Skaergaard intrusion, East Greenland. *Contributions to Mineralogy and Petrology* **112**, 428–437.

Leuthold, J., Blundy, J. D., Holness, M. B. & Sides, R. (2014). Successive episodes of reactive liquid flow through a layered intrusion (Unit 9, Rum Eastern Layered Intrusion, Scotland). *Contributions to Mineralogy and Petrology* **167**, 1021.

Madsen, S. R. (2005). A petrological and geochemical investigation of drill core 90-10 of the Skaergaard intrusion, East Greenland. MSc thesis, University of Aarhus, 88 pp. (in Danish).

Manning, C. E., Ingebritsen, S. E. & Bird, D. K. (1993). Missing mineral zones in contact metamorphosed basalts. *American Journal of Science* **293**, 894–938.

McBirney, A. R. (1989). *Geological map of the Skaergaard Intrusion, East Greenland, 1:20,000*. Department of Geology, University of Oregon.

McBirney, A. R. (1996). The Skaergaard intrusion. In: Cawthorn, R. G. (ed.) *Layered Intrusions*, Amsterdam: Elsevier, pp. 147–180.

McBirney, A. R. (2002). The Skaergaard layered series. Part VI. Excluded trace elements. *Journal of Petrology* **43**, 535–556.

McBirney, A. R. & Naslund, H. R. (1990). A discussion of Hunter & Sparks. *Contributions to Mineralogy and Petrology* **104**, 235–247.

McBirney, A. R. & Nicolas, A. (1997). The Skaergaard Layered Series: Part II. Dynamic layering. *Journal of Petrology* **38**, 569–580.

McKenzie, D. (2011). Compaction and crystallization in magma chambers: towards a model of the Skaergaard Intrusion. *Journal of Petrology* **52**, 905–930.

Meurer, W. & Boudreau, A. (1998). Compaction of igneous cumulates part II: compaction and the development of igneous foliations. *Journal of Geology* **106**, 293–304.

Morse, S. A. (1979). Kiglapait geochemistry II: petrography. *Journal of Petrology* **20**, 591–624.

Morse, S. A. (1986). Convection in aid of adcumulus growth. *Journal of Petrology* **27**, 1183–1214.

Morse, S. A. (2011). The fractional latent heat of crystallizing magmas. *American Mineralogist* **96**, 682–689.

Namur, O., Humphreys, M. C. S. & Holness, M. B. (2014). Crystallisation of interstitial liquid and latent heat buffering in solidifying gabbros: Skaergaard intrusion, Greenland. *Journal of Petrology* **55**, 1389–1427.

Naslund, H. R. (1984). Petrology of the Upper Border Series of the Skaergaard Intrusion. *Journal of Petrology* **25**, 185–212.

Nielsen, T. F. D. (2004). The shape and volume of the Skaergaard Intrusion, East Greenland: implications for mass balance and bulk composition. *Journal of Petrology* **45**, 507–530.

Nielsen, T. F. D., Tegner, C., Thy, P., Fonseca, A., Jakobsen, J. K., Kristensen, M., Simpson, J., Brooks, C. K., Kent, A. J. R., Peate, D. W. & Lesher, C. E. (2000). Retrieval of Platinova drill cores: A new Skaergaard initiative. *Transactions of the American Geophysical Union*, **81**, Fall Meeting Supplement, V21E-15.

Nielsen, T. F. D., Andersen, J. C. Ø. & Brooks, C. K. (2005). The Platinova Reef of the Skaergaard intrusion. In: Mungal, J. E. (ed.) *Exploration for Platinum Group Element Deposits. Mineralogical Association of Canada, Short Course Series* **35**, 431–455.

Nielsen, T. F. D., Olsen, S. D. & Stensgaard, B. M. (2009). Developing a 3-D model for the Skaergaard intrusion in East Greenland: constraints on structure, mineralisation and petrogenetic models. *Geological Survey of Denmark and Greenland Bulletin* **17**, 61–64.

Nielsen, T. F. D., Andersen, J. C. Ø., Holness, M. B., Keiding, J. K., Rudashevsky, N. S., Rudashevsky, V. N., Salmonsen, L. P., Tegner, C. & Veksler, I. V. (2015). The Skaergaard PGE and gold deposit: the result of *in situ* sulphide saturation and magma chamber-scale precious metal redistribution by immiscible Fe-rich melt. *Journal of Petrology* **56**, 1643–1676.

Norton, D. & Taylor, H. P. (1979). Quantitative simulation of the hydrothermal systems of crystallising magmas on the basis of transport theory and oxygen isotope data: an analysis of the Skaergaard intrusion. *Journal of Petrology* **20**, 421–486.

Riegger, O. K. & van Vlack, L. H. (1960). Dihedral angle measurements. *Transactions of the Metallurgical Society of the AIME* **218**, 933–935.

Salmonsen, L. P. & Tegner, C. (2013). Crystallisation sequence of the Upper Border Series of the Skaergaard intrusion: revised subdivision and implications for chamber-scale magma homogeneity. *Contributions to Mineralogy and Petrology* **165**, 1155–1171.

Schiffries, C. M. (1982). The petrogenesis of a platiniferous dunite pipe in the Bushveld Complex: infiltration metasomatism by a chloride solution. *Economic Geology* **77**, 1439–1453.

Shirley, D. N. (1986). Compaction of igneous cumulates. *Journal of Geology* **94**, 795–809.

Smith, C. E. (1964). Some elementary principles of polycrystalline microstructure. *Metallurgical Reviews* **9**, 1–48.

Sonnenthal, E. L. (1992). Geochemistry of dendritic anorthosites and associated pegmatites in the Skaergaard Intrusion, East Greenland: evidence for metasomatism by a chlorine-rich fluid. *Journal of Volcanology and Geothermal Research* **52**, 209–230.

Sparks, R. S. J., Kerr, R. C., McKenzie, D. P. & Tait, S. R. (1985). Postcumulus processes in layered intrusions. *Geological Magazine* **122**, 555–568.

Stickels, C. A. & Hücke, E. E. (1964). Measurement of dihedral angles. *Transactions of the Metallurgical Society of the AIME* **230**, 795–801.

Svennevig, K. & Guarnieri, P. (2012). From 3D mapping to 3D modelling: a case study from the Skaergaard intrusion, southern East Greenland. *Geological Survey of Denmark and Greenland Bulletin* **26**, 57–60.

Tait, S. & Jaupart, C. (1992). Compositional convection in a reactive crystalline mush and melt differentiation. *Journal of Geophysical Research* **97**, 6735–6756.

Tait, S. R., Huppert, H. E. & Sparks, R. S. J. (1984). The role of compositional convection in the formation of adcumulate rocks. *Lithos* **17**, 139–146.

Taylor, H. P. & Forester, R. W. (1979). An oxygen and hydrogen isotope study of the Skaergaard intrusion and its country rocks: a description of a 55 M.Y. old fossil hydrothermal system. *Journal of Petrology* **20**, 355–419.

Tegner, C. (1997). Iron in plagioclase as a monitor of the differentiation of the Skaergaard intrusion. *Contributions to Mineralogy and Petrology* **128**, 45–51.

Tegner, C. & Cawthorn, R. G. (2010). Iron in plagioclase in the Bushveld and Skaergaard intrusions: implications for iron contents in evolving basic magmas. *Contributions to Mineralogy and Petrology* **159**, 719–730.

Tegner, C., Wilson, J. R. & Cawthorn, R. G. (1994). The dunite–clinopyroxenite pegmatoidal pipe, Tweefontein, Eastern Bushveld Complex, South Africa. *South African Journal of Geology* **97**, 415–430.

Tegner, C., Thy, P., Holness, M. B., Jakobsen, J. K. & Lesher, C. E. (2009). Differentiation and compaction in the Skaergaard intrusion. *Journal of Petrology* **50**, 813–840.

Tharp, T. M., Loucks, R. R. & Sack, R. O. (1998). Modeling compaction of olivine cumulates in the Muskox intrusion. *American Journal of Science* **298**, 758–790.

Thompson, R. N. & Patrick, D. J. (1968). Folding and slumping in a layered gabbro. *Geological Journal* **6**, 139–146.

Toplis, M. J. & Carroll, M. R. (1995). An experimental study of the influence of oxygen fugacity on Fe–Ti oxide stability, phase relations, and mineral–melt equilibria in ferro-basaltic systems. *Journal of Petrology* **36**, 1137–1170.

Toplis, M. J. & Carroll, M. R. (1996). Differentiation of ferro-basaltic magmas under conditions open and closed to oxygen: implications for the Skaergaard intrusion and other natural systems. *Journal of Petrology* **37**, 837–858.

Turbeville, B. N. (1993). Sidewall differentiation in an alkalic magma chamber: evidence from syenite xenoliths in tuffs of the Latera caldera, Italy. *Geological Magazine* **130**, 453–470.

Wager, L. R. (1960). The major element variation of the layered series of the Skaergaard intrusion and a re-estimation of the average compositions of the hidden layered series and of the successive residual magmas. *Journal of Petrology* **1**, 364–398.

Wager, L. R. & Brown, G. M. (1968). *Layered Igneous Rocks*. Oliver & Boyd.

Wager, L. R. & Deer, W. A. (1939). Geological investigations in East Greenland. Part III. The petrology of the Skaergaard intrusion, Kangerdlussuaq, East Greenland. *Meddelelser om Grønland* **105**.

Wager, L. R., Brown, G. M. & Wadsworth, W. J. (1960). Types of igneous cumulates. *Journal of Petrology* **1**, 73–85.

Wright, T. L., Kinoshita, W. T. & Peck, D. L. (1968). March 1965 eruption of Kilauea Volcano and the formation of Makaopuhi Lava Lake. *Journal of Geophysical Research* **73**, 3181–3205.

Wyllie, P. J. (1963). Effects of the changes in slope occurring on liquidus and solidus paths in the system diopside–anorthite–albite. International Mineralogical Association: Papers and Proceedings of the Third General Meeting. Special paper, Mineralogical Society of America. No.1.